ACS NANO
Cite This: ACS Nano XXXX, XXX, XXX−XXX
www.acsnano.org
ARTICLE

Tumor Ablation and Therapeutic Immunity Induction by an Injectable Peptide Hydrogel

Honglin Jin,[†,⊥] Chao Wan,[†,⊥] Zhenwei Zou,[†,⊥] Guifang Zhao,[†] Lingling Zhang,[†] Yuanyuan Geng,[†] Tong Chen,[†] Ai Huang,[†] Fagang Jiang,[‡] Jue-Ping Feng,[§] Jonathan F. Lovell,[∥] Jing Chen,[*,†] Gang Wu,[*,†] and Kunyu Yang[*,†]

[†]Cancer Center, Union Hospital and [‡]Department of Ophthalmology, Union Hospital, Tongji Medical College, Huazhong University of Science and Technology, Wuhan 430022, China

[§]Department of Oncology, PuAi Hospital, Tongji Medical College, Huazhong University of Science and Technology, Wuhan 430034, China

[∥]Department of Biomedical Engineering, University at Buffalo, State University of New York, Buffalo, New York 14260, United States

Supporting Information

ABSTRACT: **Immunosuppressive tumor microenvironments (TMEs) create tremendous obstacles for an effective cancer therapy. Herein, we developed a melittin-RADA$_{32}$ hybrid peptide hydrogel loaded with doxorubicin (DOX) for a potent chemoimmunotherapy against melanoma through the active regulation of TMEs. The formed melittin-RADA$_{32}$-DOX (MRD) hydrogel has an interweaving nanofiber structure and exhibits excellent biocompatibility, controlled drug release properties both *in vitro* and *in vivo*, and an enhanced killing effect to melanoma cells. A single-dose injection of MRD hydrogel retarded the growth of primary melanoma tumors by more than 95% due to loaded melittin and DOX, with concomitant recruitment of activated natural killer cells in the tumors. Furthermore, MRD hydrogel can activate dendritic cells of draining lymph nodes, specifically deplete M2-like tumor-associated macrophages (TAMs), and produce active, cytotoxic T cells to further defend the cells against remaining tumors, providing potent anticancer efficacy against subcutaneous and metastatic tumors *in vivo*. Multidose injection of MRD hydrogel eliminated 50% of the primary tumors and provided a strong immunological memory effect against tumor rechallenge after eradication of the initial tumors. Owing to its abilities to perform controlled drug release, regulate innate immune cells, deplete M2-like TAMs, direct anticancer and immune-stimulating capabilities, and reshape immunosuppressive TMEs, MRD hydrogel may serve as a powerful tool for anticancer applications.**

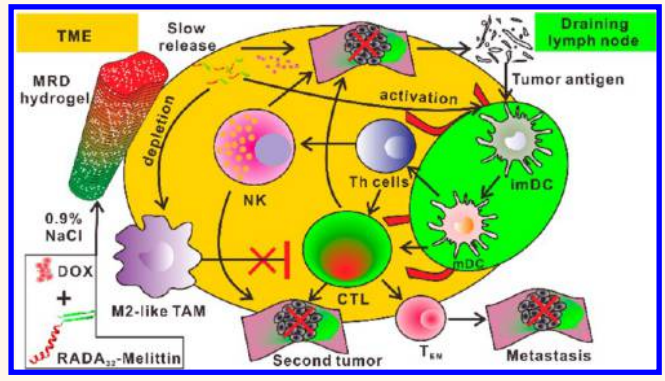

KEYWORDS: *chemoimmunotherapy, melanoma treatment, biomaterials, tumor microenvironment, hydrogel, macrophage depletion, cytotoxic T cells*

A main pursuit of cancer therapy is to eradicate or dramatically block the growth of primary tumors, control metastases, and prevent tumor relapses after eradication of the primary tumors. However, the presence of complicated and heterogeneous tumor microinvironments (TME) hinders traditional therapies (such as surgery, chemotherapy, and radiotherapy); all failed to accomplish this goal.[1−3] Increasing evidence has confirmed that immunosuppressive TMEs are often highly correlated with drug resistance, radioresistance, and poor prognosis in patients.[4−6] Thus, remodeling an immunosuppressive TME toward an immunosupportive one has been considered to be one of the most promising approaches in treating malignant tumors.[7,8] Despite that many promising attempts have been made in altering TMEs through immunotherapy, for example, by applying cytokines,[9,10] checkpoint-blockade therapy,[11,12] cancer nanovaccines,[13−15] and cell-based immunotherapy,[16,17] the overall antitumor outcome remains unsatisfactory. Moreover, most of these therapies have limitations, such as large individual variations in therapeutic responses, extremely high costs, significant side effects from systemic dosing, and poor pharmacokinetic profiles *in vivo*, which need to be improved.[2,18] Thus, the development of a simple, robust, and biocompatible antitumor approach that effectively shapes the TME is urgently needed.

Received: November 16, 2017
Accepted: March 20, 2018
Published: March 20, 2018

DOI: 10.1021/acsnano.7b08148
ACS Nano XXXX, XXX, XXX−XXX

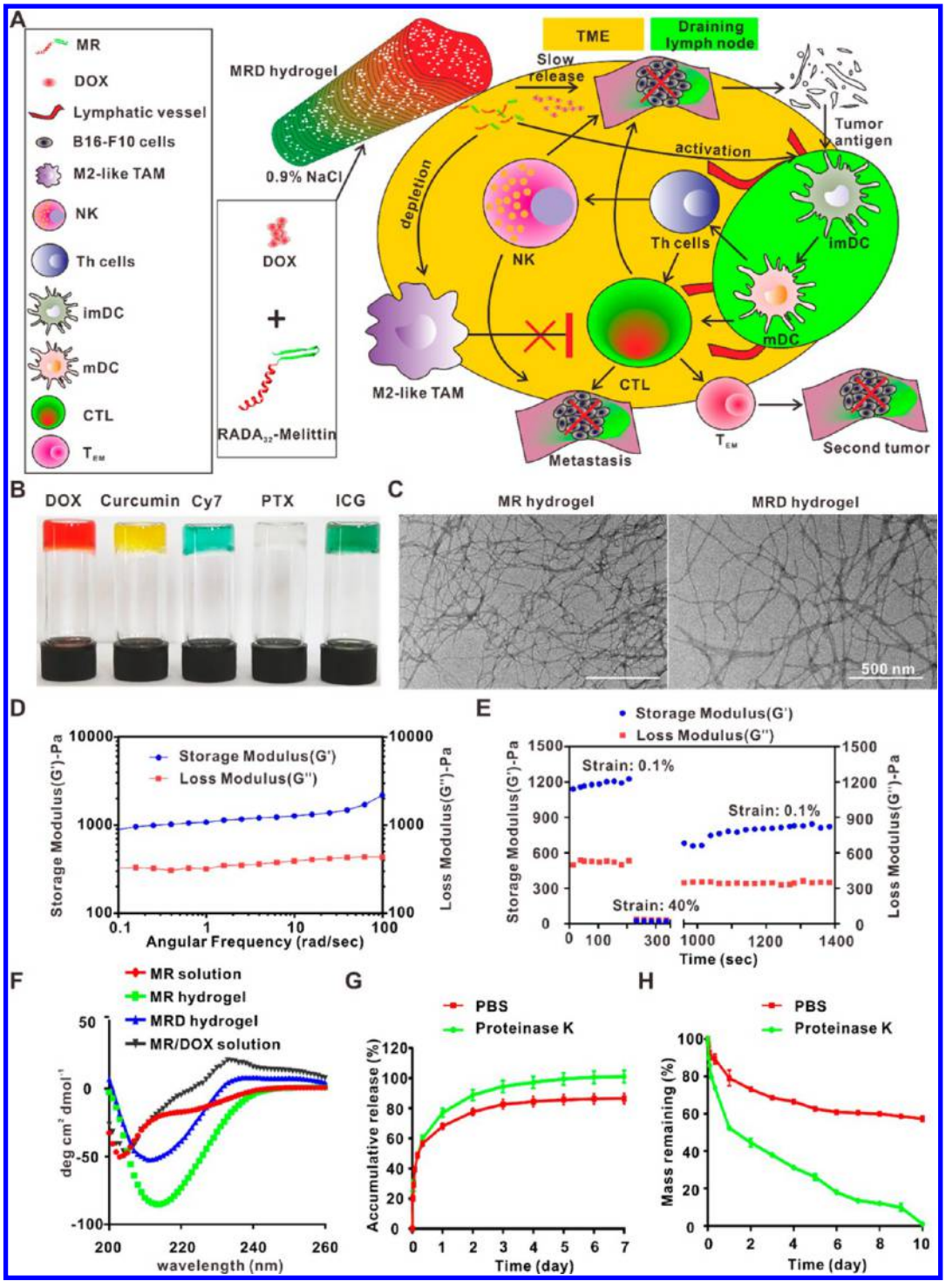

Figure 1. Preparation and characterization of MRD hydrogel. (A) Mechanism of MRD hydrogel-mediated antitumor effects against melanoma. (B) Photographs of MRD hydrogels loaded with various agents. (C) TEM images of MR and MRD hydrogel. The scale bar represents 500 nm. (D) Frequency sweep rheological analysis of the MRD hydrogel. Measurements were performed at a constant strain of 0.1%. (E) Step-strain time-dependent rheological analysis of the MRD hydrogel. Measurements were performed at a fixed angular frequency of 1 rad/s. (F) CD images of MR solution, MR peptide, MR hydrogel, and MRD hydrogel. (G) Comparison of the release profile of MRD hydrogel-loaded DOX in the presence or absence of proteinase K. (H) Comparison of the MR hydrogel release profile in the presence or absence of proteinase K.

TMEs are composed of blood, lymphatic vessels, tumor cells, and a variety of nonmalignant host cells, including fibroblasts and a large population of resident and trafficking immune cells.[19,20] Among these components, tumor and immune cells play a central role in mediating tumor surveillance or tumor progression. Therefore, for therapeutic approaches to be effective, at least three main factors need to be considered. First, the rapid growth of primary tumors needs to be effectively controlled, which may result in a large tumor burden, invasion of surrounding tissues, and a high risk of distal metastases.

DOI: 10.1021/acsnano.7b08148
ACS Nano XXXX, XXX, XXX−XXX

Another benefit of rapid tumor killing is that cell necrosis mediated by therapeutics may provide a tumor antigen pool, which is essential for the generation of antigen-specific immune responses.[21] Second, TMEs could be altered to treat cancer by stimulating the innate immune system and generating an adaptive immunity.[22] This may require recruitment and activation of effector immune cells of the TMEs, such as natural killer cells (NKs),[23,24] a type of cytotoxic lymphocytes critical to the innate immune system, and dendritic cells (DCs),[13,25] the most powerful antigen-presenting cells (APCs) that are specialized in initiating T-cell adaptive immunity. In fact, recent studies suggested that $CD8^+$ T cells and NKs are likely to be the most important immune cells responsible for anticancer effects.[26] Finally, TMEs can produce an immunosuppressive environment by releasing soluble cytokine mediators and attracting immunosuppressive cell types, such as tumor-associated macrophages (TAMs), regulatory T cells (Tregs), and myeloid-derived suppressor cells (MDSCs).[27,28] It has been suggested that the presence of a large population of immunosuppressive cells in TMEs is often associated with treatment resistance and poor clinical prognosis.[29,30] Recent studies have shown that depletion of these immunosuppressive cells leads to enhanced anticancer efficacy.[27] Taken together, all these considerations, new approaches for cancer therapy demand rapid inhibition of primary tumors and control over the TMEs to prime effector immune cells and deplete immunosuppressive cells.

One option to integrate all these properties into one system is the use of hydrogels, which are defined as water-swollen and cross-linked polymeric networks produced by the simple reaction of one or more monomers. Due to their large drug loading and controlled release capacity as well as biocompatibility, several types of hydrogels have been tested for chemoimmunotherapy of cancer.[31,32] These hydrogels normally contain a hydrogel scaffold into which therapeutic drugs and immune-regulating molecules are incorporated. For example, Li *et al.* have reported an alginate hydrogel loaded with celecoxib and programmed death-1 monoclonal antibody, which shows strong antitumor effects by remodeling immune, inflammatory, and angiogenic TMEs.[31] Wu *et al.* have reported interleukin-15 and cisplatin co-encapsulated thermosensitive polypeptide hydrogels for a combined chemoimmunotherapy of melanoma.[33] However, curative effects have not been observed in these therapeutic strategies, possibly due to the lack of an advanced rapid tumor-killing mechanism beyond the hydrogel-loaded therapeutic drugs. Additionally, in these platforms, the hydrogel scaffold itself only acts as a drug-releasing depot, but has no antitumor function or immune-stimulating ability. Thus, we hypothesize that an ideal TME-remodeling hydrogel scaffold should accommodate both antitumor- and immune-stimulating properties.

RADA16-I is a synthetic amphiphilic peptide with the sequence RADARADARADARADA that can self-assemble into a peptide nanofiber hydrogel.[34,35] Melittin, a cationic polypeptide composed of 26 amino acids derived from bee venom, is an extremely potent anticancer agent, with the hemolysis effect as main limitation for its *in vivo* application.[36] In this study, we synthesized a melittin-$RADA_{32}$-doxorubicin (DOX) hydrogel (MRD hydrogel), which carries the melittin peptide in the peptide hydrogel scaffold, introduced by a peptide fusion strategy, and DOX in the hydrogel matrix. We demonstrated that the loading of melittin into a hydrogel scaffold dramatically reduces the side effects and, more importantly, enhances the antitumor efficacy and immune responses. The dual delivery of melittin and DOX from the MRD hydrogel elicits a potent and sustained antitumor effect, which is accompanied by an increased innate immunity, reduced immunosuppression, and activation of effector T cells (Figure 1A).

RESULTS

Preparation and Characterization of Cargo-Loaded Melittin-$RADA_{32}$ Hydrogel. Melittin is a cationic peptide derived from bee venom with the sequence GIGAVLKVLTTGLPALISWIKRKRQQ. It has a strong ability to disrupt membrane systems, such as cell membranes, liposome lipid membranes, and red blood cell (RBC) membranes.[37] Due to its strong hemolysis effect, *in vivo* applications have been a tremendous challenge. To prepare a melittin-encapsulated peptide hydrogel, we designed the melittin-containing fusion peptide melittin-$RADA_{32}$ (RADARADARADARADA-RADARADARADARADARADARADA-GG-GIGAVLKVLTT-GLPALISWIKRKRQQ-NH_2), denoted as MR peptide, in which melittin is linked to $RADA_{32}$ through a GG linker. As shown in Figure S1, the MR peptide gelates at a concentration of 0.5−2% in the presence of 0.9% NaCl (w/w), while no hydrogel was produced in the absence of NaCl, suggesting that the MR peptide acts as a building block of the peptide hydrogel under physiological conditions. In this way, melittin was successfully encapsulated into the peptide hydrogel scaffold. For stable loading of various active agents in the gel matrix, we chose an MR peptide concentration of 1% (w/w) for the following studies. Following changes of pH, we observed that the MR peptide could gelate at pH 4.0−7.5, while no hydrogel was formed at pH 8.5 (Figure S2). The MR hydrogel became a clear injectable solution when subjected to vigorous shaking (Figure S3), showing its thixotropic nature. As shown in Figure 1B, the resulting MR hydrogel platform is well suited for the loading of a broad range of hydrophilic and hydrophobic functional molecules, including chemotherapeutics, such as DOX, curcumin, and docetaxel, and optical imaging agents, such as Cy7 and indocyanine green (ICG). More crucially, the efficiencies for loading these agents into the MR hydrogel all reach nearly 100%, which may provide great benefits for the drug encapsulation efficiency when applied for drug delivery.[38] To demonstrate the potential of dual drug-loaded peptide hydrogels in treating cancer in a proof-of-concept study, we chose to investigate the treatment of melanoma with the melittin-$RADA_{32}$-DOX (MRD) hydrogel.

Size and shape of the MRD hydrogel were analyzed by transmission electron microscopy (TEM), and its secondary structure was analyzed by circular dichroism (CD). As revealed by TEM, MR, and MRD hydrogels self-assembled into networks of interweaving nanofibers with diameters of 10.5 ± 1.8 and 21.2 ± 4.2 nm, respectively (Figure 1C). Figure 1D shows rheological characterization of the MRD hydrogel. Both the storage modulus (G') and loss modulus (G'') of the MRD hydrogel were weakly dependent on frequency (0.1−100 rad/s) when keeping strain constant at 0.1%, indicating formation of a stable hydrogel. To confirm the injectable nature of a gel-like material, a time-dependent step-strain rheological experiment was performed.[39] In this experiment, the MRD hydrogel was first tested under low constant strain of 0.1% for the first 200 s, followed with a higher strain of 40% to rupture the gel matrix. Thereafter, we adjusted the strain to a constant low level of 0.1%, and the restoration process was recorded (Figure 1E). In

DOI: 10.1021/acsnano.7b08148
ACS Nano XXXX, XXX, XXX−XXX

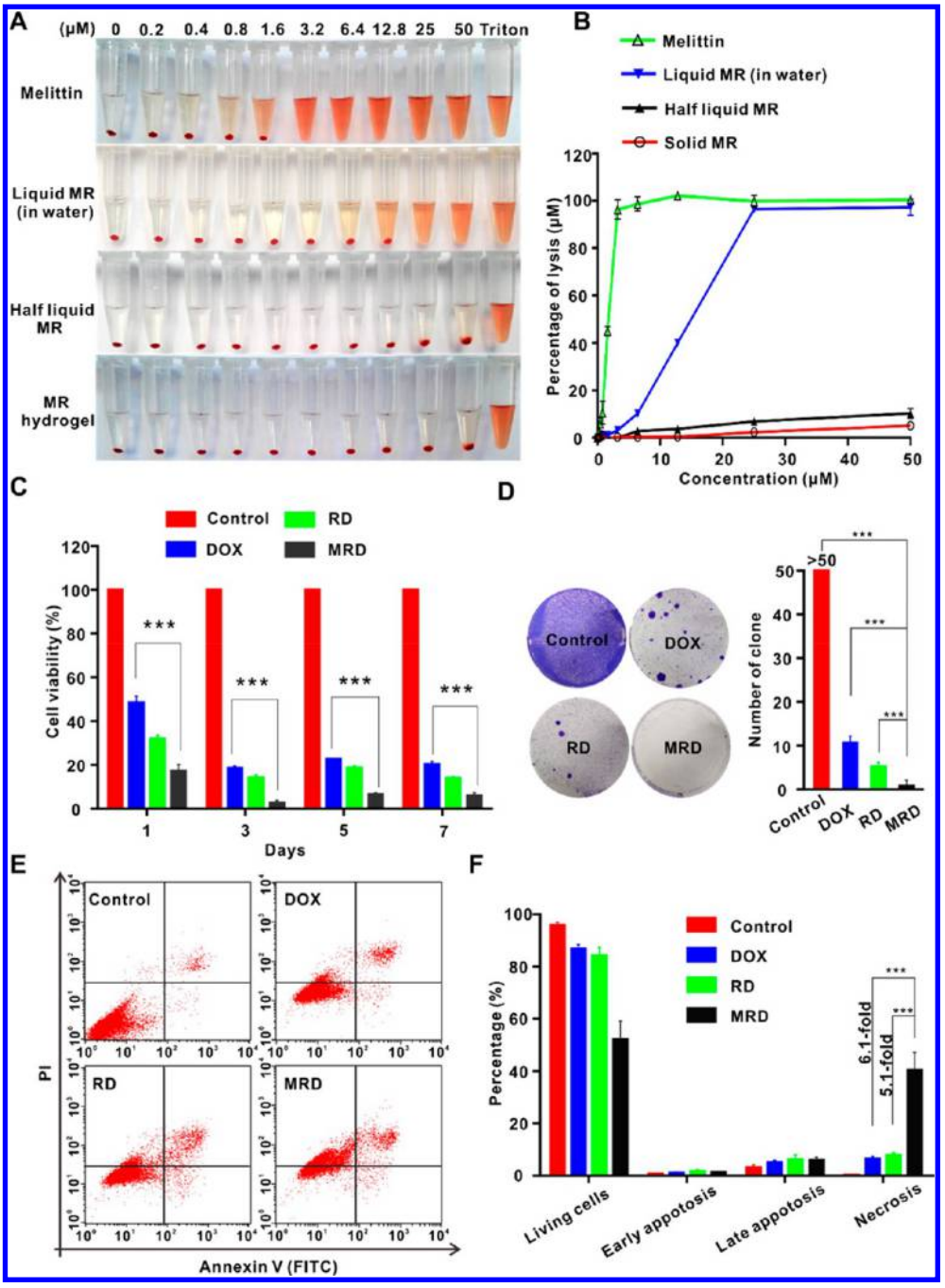

Figure 2. ***In vitro*** **antitumor effects of MRD hydrogel. (A) Hemolysis effects on RBCs of liquid MR peptide (in water), liquid MR peptide (in saline), MR hydrogel, and free melittin. (B) Quantitative data from the hemolysis measurement described in (A). Data are presented as the mean ± standard error of the mean (SEM; *n* = 3). The hemolysis rate for the 1% Triton x-treated group was set as positive control (100%). (C) Cell viability measurement using the CCK-8 assay. (D) Clone formation analysis (left panel: representative images of cell clones treated with PBS, DOX, RD, or MRD hydrogel; right panel: quantification of clone formation; *n* = 3). (E,F) Flow cytometry measurement of cell apoptosis induced by DOX, RD, or MRD hydrogel. Data are presented as the mean ± SEM (*n* = 3).**

these conditions, the hydrogel could gradually recover most of its original strength at 1000 s after the withdrawal of the large strain, suggesting a good rheological nature for injectable applications. CD measurements showed negative maximum molar residue ellipticities at 216 nm for both MR and MRD hydrogels, which is characteristic for a β-sheet structure. In contrast, MR and MRD solutions (without NaCl) exhibited no obvious peak at 216 nm, indicating that the fusion of melittin and $RADA_{32}$ peptide and the loading of DOX into the MR hydrogel do not hinder β-sheet formation (Figure 1F). We next examined the release rate of DOX from the MRD hydrogel in the presence or absence of proteinase K, which digests a broad range of peptides and natural proteins. Results showed that in the presence of proteinase K, DOX loaded into the MRD hydrogel had a release rate of 77.1% at 24 h, 88.8% at 48 h, and maintained stable after 72 h (Figure 1G). In the absence of proteinase K, this value was 68.0% at 24 h and 77.7% at 48 h, suggesting that the addition of proteinase K obviously accelerated the release rate of DOX. Additionally, we measured the release level of backbone peptide from the MR hydrogel.

DOI: 10.1021/acsnano.7b08148
ACS Nano XXXX, XXX, XXX−XXX

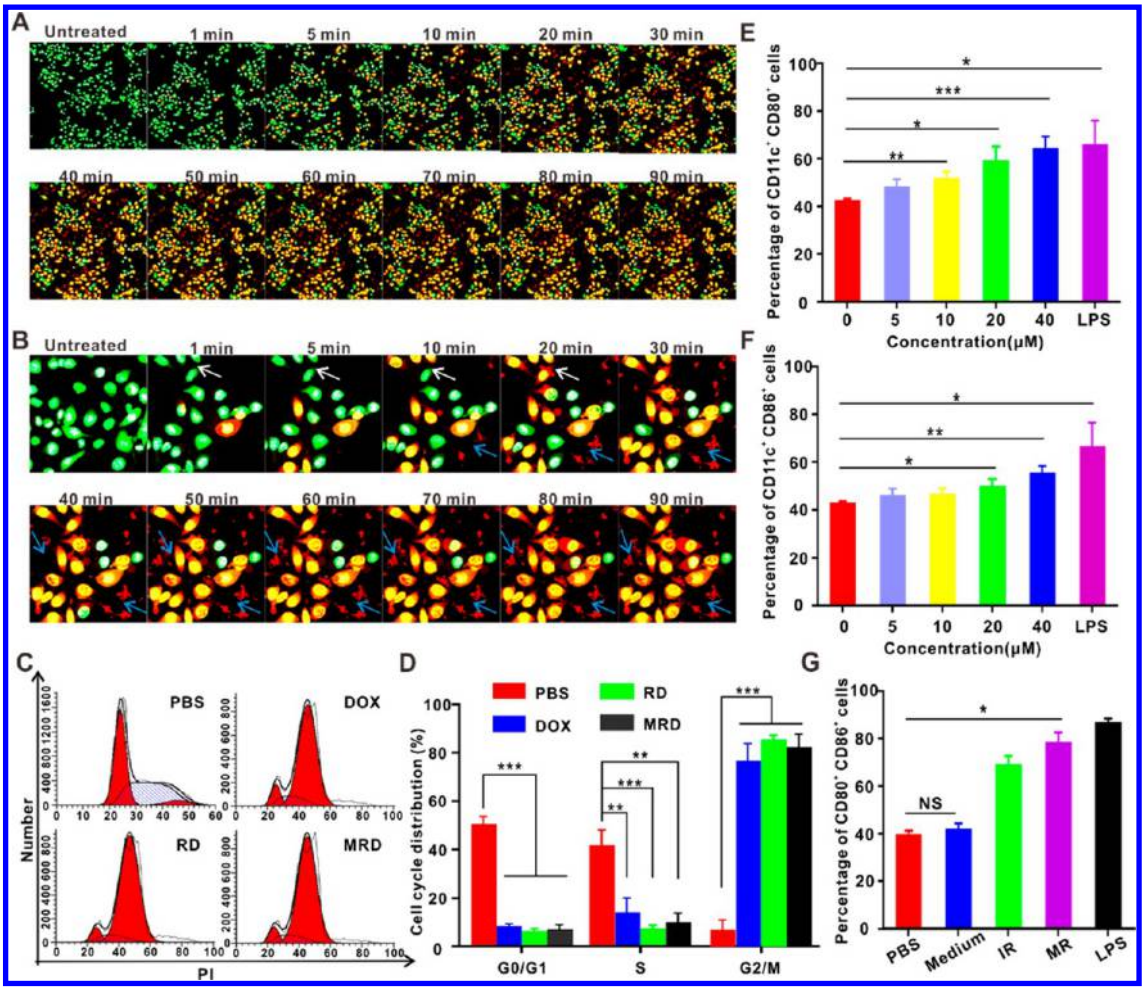

Figure 3. ***In vitro*** **antitumor mechanisms and immune-stimulating effects of MRD hydrogel. (A) Confocal real-time fluorescence images of B16-GFP cells treated with the MR hydrogel. For nuclear staining, the cells were prestained with Hoechst 33342. (B) Zoom-in images of the confocal studies presented in (A). (C) Flow cytometry of cell cycle changes induced by DOX, RD, or MRD hydrogel. (D) Quantitative data from (C). (E,F) Evaluation of the expression levels of the DC surface markers CD80 and CD86 upon MR hydrogel treatment. Data are presented as the mean ± SEM (n = 3). (G) Effects of MR hydrogel-induced tumor cell death on the maturation of DCs. Ionizing radiation (IR) was used as a positive control for stimulation of DCs.**

According to Figure 1H, the MR hydrogel exhibited a slower backbone peptide release rate than obtained in the presence of proteinase K. At day 10, 57.3% of the MR hydrogel remained, indicating a slow release rate of the MR hydrogel. In contrast, the MR hydrogel had been completely released at this time point in the presence of proteinase K due to digestion, indicating an excellent biodegradability of this hydrogel (Figure 1H). Together, these results suggest that we successfully synthesized a biodegradable, controlled-releasable, and DOX- and melittin-loaded peptide hydrogel.

In Vitro **Antitumor Effect of MRD Hydrogel.** As melittin shows strong hemolysis as a side effect, we explored whether this effect was reduced in the MR hydrogel by evaluating its ability to disrupt RBCs. We used 1% Triton X-100 as a positive control and compared four different forms of melittin complexes: (1) free melittin; (2) liquid MR peptide in which the hydrogel was dissolved in water; (3) half-liquid MR peptide in which the hydrogel peptide was dissolved in saline without sufficient time for gelation; and (4) MR hydrogel. As shown in Figure 2A,B, the concentrations of free melittin and liquid MR peptide required for complete lysis of RBCs were 3.2 and 25 μM, respectively, while more than 50 μM of half-liquid MR and MR hydrogel were required for complete RBC lysis. These results suggest that linking melittin to the $RADA_{32}$ peptide dramatically decreased the hemolysis effect of melittin, which was further reduced by the formation of the solid MR hydrogel.

Next, we investigated the cytotoxicity of the MRD hydrogel. The antitumor efficacy of the MRD hydrogel against melanoma B16-F10 cells was tested by a CCK-8 assay, clone formation, and apoptosis analysis. Prior to these studies, we observed that the dispersion status had an impact on cell-killing by the MR hydrogel. If the MR hydrogel was directly added to cells, its form was maintained as a clustered, solid MR hydrogel. However, when subjected to repeat pipetting, the MR hydrogel was disrupted and became fragmented (Figure S4A). As revealed by the CCK-8 assay, the fragmented RADA hydrogel group (without DOX loading) had no cytotoxic effects to B16-F10 cells, while fragmented MR hydrogel demonstrated potent antitumor effects within the same test concentrations (0−16 μM) (Figure S4B). We further examined cell-killing by the MR hydrogel in various cell lines including B16-F10 cells, DCs and L929 murine fibroblasts. Overall, the half maximal inhibitory concentration (IC_{50}) in the solid MR hydrogel-treated groups was ~6−7 times higher than that of the fragmented MR

DOI: 10.1021/acsnano.7b08148
ACS Nano XXXX, XXX, XXX−XXX

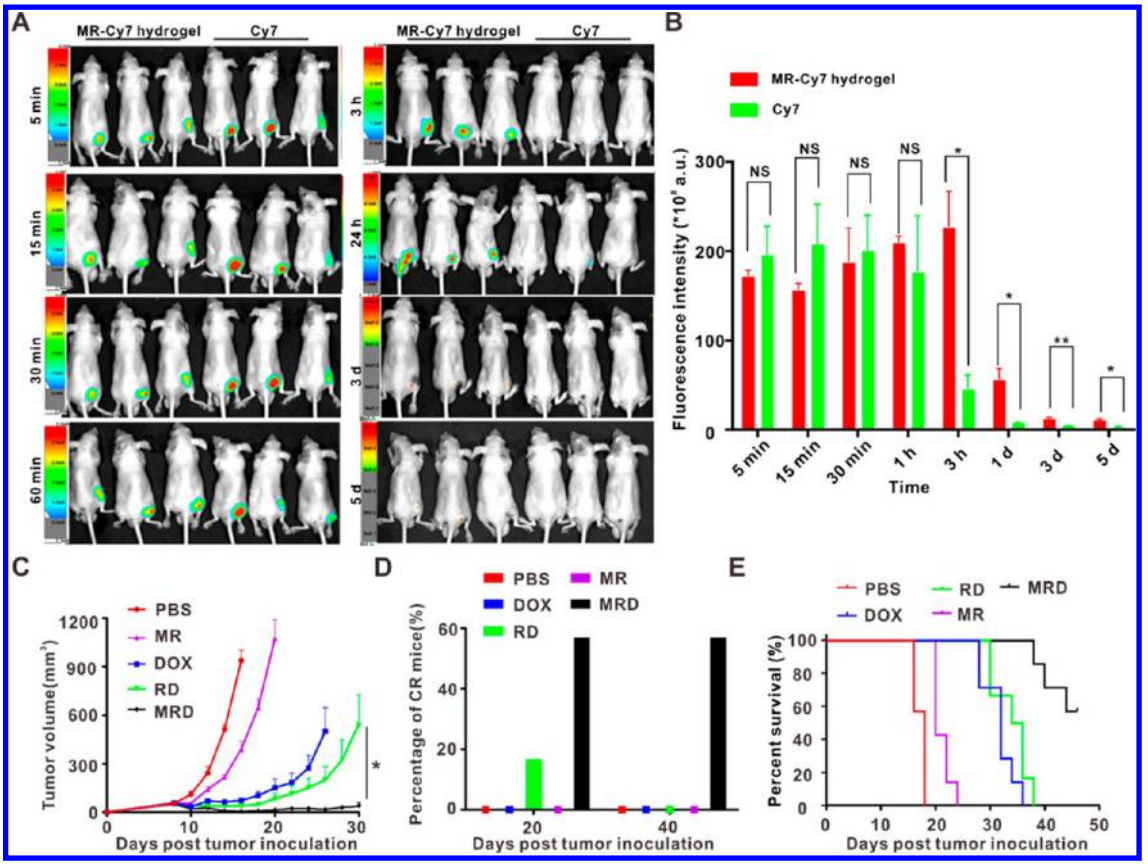

Figure 4. ***In vivo*** **drug-release profile and antitumor effects of MRD hydrogel. (A)** ***In vivo*** **NIR fluorescence imaging of the distribution of MR-Cy7 hydrogel and Cy7 dye after subcutaneous injection at various time points. (B) Quantitative data from (A). (C) Tumor growth curves for mice intratumorally injected with PBS, DOX, RD, MR, or MRD hydrogel. Data are presented as the mean ± SEM (*n* = 6−7). (D) Percentages of the tumor-bearing mice that had complete regression (CR) in the corresponding treatment groups. (E) Survival percentages in the corresponding treatment groups described in (C).**

hydrogel, and these killing effects were not cell-line specific (Figure S4C−E). For consistency, we used the solid MR hydrogel for all subsequent studies unless noted otherwise.

As shown in Figure 2C, the $RADA_{16}$-DOX (RD) hydrogel group showed cell inhibition rates of 68, 86, 81, and 86% at days 1, 3, 5, and 7, respectively, which were much higher than those of the DOX group (51, 81, 77, and 80%, respectively, at the same days) under the same conditions (2 μM of DOX), confirming the advantage of the peptide hydrogel as a controlled drug release vehicle for enhanced antitumor efficacy. More crucially, the MRD hydrogel group showed significantly higher cell death rates (83, 97, 93, and 94% at days 1, 3, 5, and 7, respectively) than the RD hydrogel group at all tested time points, suggesting that the backbone-loading of melittin into the RD hydrogel conferred enhanced antitumor efficacy. Consistent with the results of the CCK-8 assay, clone formation analysis showed that the cell clones in the MRD hydrogel-treated group were almost completely eliminated, displaying significantly less clones than the other groups (Figure 2D). These results indicate an enhanced and long-term inhibitory effect of the MRD hydrogel against B16-F10 cells. Moreover, as revealed by flow cytometry analysis, the percentage of necrotic cells reached 40.5% for the MRD hydrogel group, which is 5.1- and 6.1-fold higher than the RD hydrogel and DOX group, respectively (Figure 2E,F). These results suggest that the MRD hydrogel facilitates cell necrosis, which is the main cause of *in vitro* cell death resulting from the MRD hydrogel.

In Vitro **Antitumor Mechanisms and Immune-Stimulating Abilities.** To demonstrate the therapeutic mechanisms of MR hydrogel-mediated cell death, real-time confocal imaging studies were performed using green fluorescent protein (GFP)-expressing B16-F10 cells (B16-GFP). In this study, propidium iodide (PI) was added to stain dead cells (red signal) because PI cannot readily penetrate the cell membranes of viable cells. Before adding the MR hydrogel, B16-GFP showed only a green fluorescence signal. When the MR hydrogel was added, a small portion of the cells showed a yellow signal (merge of green and red colors; Figure 3A) within 5 min. After 10 min, more and more cells displayed yellow signals and gradually became the dominant cell type, suggesting that a large number of cells were destroyed. At 90 min, more than 75% of cells were killed by the MR hydrogel (Figure S5). These data suggest that MR hydrogel-mediated cell death is a rapid process. Furthermore, we typically observed membrane swelling, as revealed by the development of balloon-like bumps in the cell membranes (Figure 3B; white arrow). Additionally, we observed the formation of micrometer-scale aggregates (Figure 3B; blue arrow), which are likely complexes of PI and intracellular nucleic acids, indicating the exposure of intracellular content. These data suggest that MR hydrogel treatment resulted in cell membrane disruption and release of intracellular content.

As DOX interacts with DNA and inhibits the intercellular biosynthesis of macromolecules, we next investigated whether DOX loaded into peptide hydrogel retains the ability to

DOI: 10.1021/acsnano.7b08148
ACS Nano XXXX, XXX, XXX−XXX

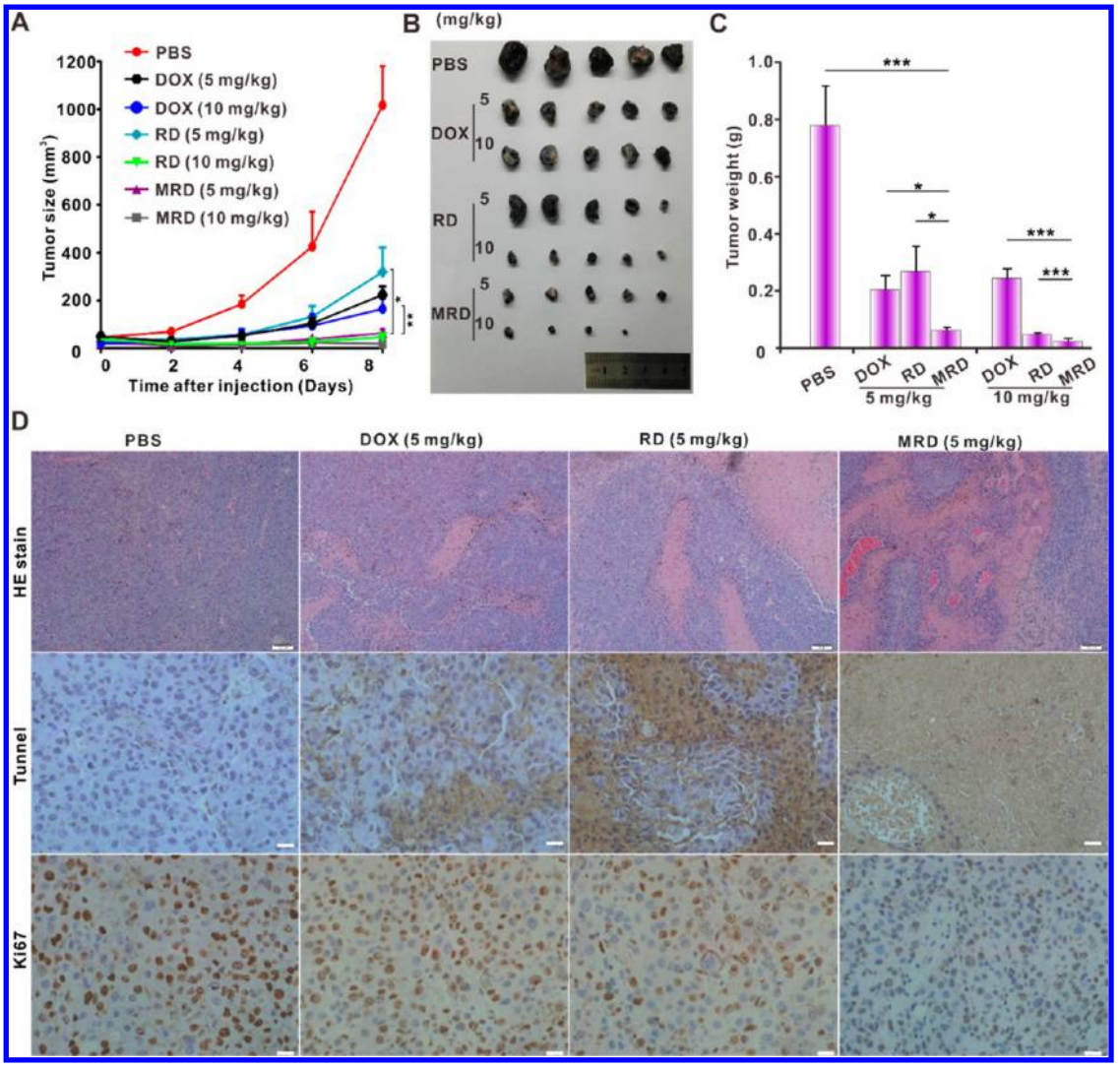

Figure 5. Evaluation of the *in vivo* antitumor efficacy of MRD hydrogel after peritumoral injection. (A) Tumor growth curves for mice peritumorally injected with PBS, DOX, RD, or MRD hydrogel. Data are presented as the mean ± SEM (n = 5). (B) Photograph of dissected tumor samples. (C) Quantification of the tumor weights in each group. (D) Representative histological examinations of the dissected tumors using HE staining, TUNEL assay, and Ki67 staining. The scale bar represents 200 μm.

interfere with the cell cycle progression in B16-F10 cells. Flow cytometry showed that cells treated with DOX, RD hydrogel, or MRD hydrogel had very similar cell cycle profiles (Figure 3C) with a much higher cell portion arrested in the G2/M phase and significantly reduced the amount of cells distributed in the S phase (Figure 3D). This shows that the MRD hydrogel has the ability to inhibit the cell cycle progression.

As DCs serve as master regulators of T-cell adaptive immunity, we next explored whether the MR hydrogel can promote the maturation of DCs *in vitro*. For this experiment, immature bone marrow-derived dendritic cells (BMDCs) were harvested and exposed to various MR hydrogel concentrations for 24 h. To characterize the maturation of DCs, the surface marker expression level was assessed using flow cytometry. We found that exposure to the MR hydrogel augmented the expression levels of the surface markers CD80 and CD86 in a concentration-dependent manner (Figure 3E,F), which was concomitant with increased levels of secreted cytokines associated with DC maturation, such as IL2, IL-6, IL12, and TNFα detected in the cell supernatants (Figure S6). At an MR hydrogel concentration of 40 μM, the maturation effect was close to that of lipopolysaccharide (LPS; positive control), a well-known agent that effectively stimulates DC maturation. Additionally, we observed that the cell supernatants from MR hydrogel-treated B16-F10 cells could promote DC maturation (Figure 3G) and that this effect was time dependent (0−48 h; Figure S7), indicating that MR hydrogel-induced tumor cell death had an active role in promoting DC maturation. Altogether, these results demonstrate a facilitative role of the MR hydrogel on DC maturation.

***In Vivo* Drug-Release Profile and Anticancer Effect of MRD Hydrogel.** After confirming the dramatically reduced hemolysis effect and strong antitumor effect of the MRD hydrogel *in vitro*, we further assessed its *in vivo* release profile. For the *in vivo* release study of MRD hydrogel-loaded DOX, we loaded the MR hydrogel with the fluorescence dye Cy7, which was chosen for its similar molecular weight and water solubility to DOX to mimic the biodistribution of the MRD hydrogel. After subcutaneous injection of 50 μL MR-Cy7 hydrogel into mice, its real-time biodistribution was monitored by near-infrared (NIR) fluorescence imaging. As shown in Figure 4A, both MR-Cy7 hydrogel and Cy7 dye-treated mice displayed

DOI: 10.1021/acsnano.7b08148
ACS Nano XXXX, XXX, XXX−XXX

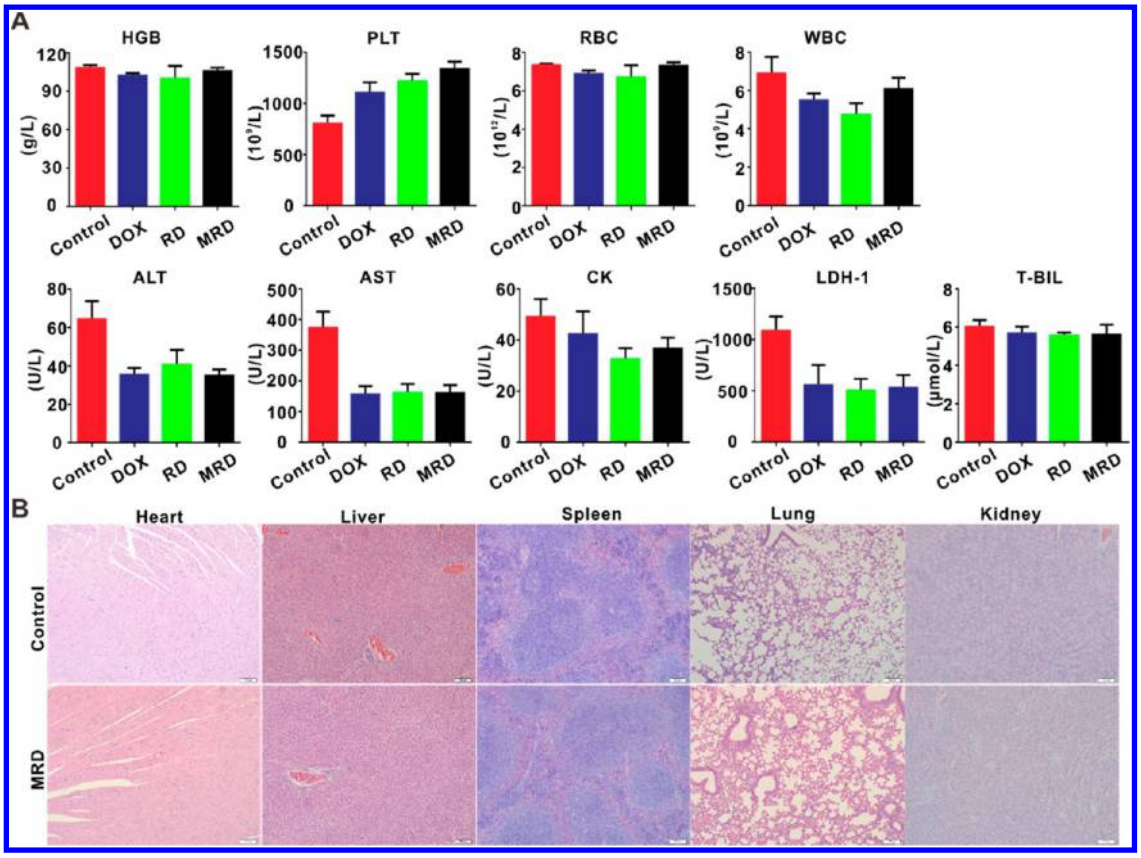

Figure 6. Hemanalysis and biochemical analyses. (A) Hemanalysis was performed on blood withdrawn from mice on day 8 post drug treatment. Data are presented as the mean ± SEM (n = 3). (B) Representative histological examinations of the main organs with HE staining. Images of the main organs from mice injected with PBS, DOX, RD, or MRD hydrogel. The scale bar represents 200 μm.

strong fluorescence signals within the first hour post-injection, and no significant difference was observed at these time points (Figure 4B). However, at 3 and 24 h, the fluorescence signals in the MR-Cy7 hydrogel group were 4.9 and 7.7-fold, respectively, stronger than those in the Cy7 group. These differential fluorescence signals were also observed at 3 and 5 d post-injection. These results suggest that an enhanced sustained release of the cargo could be achieved through MR hydrogel loading.

Due the controlled drug delivery, functional hydrogel biomaterials have great promise for localized drug delivery. To demonstrate the therapeutic potential of the MRD hydrogel, we carried out preliminary experiments using the MRD hydrogel for treating established subcutaneous B16-F10 tumor-bearing mice. When the tumor volume reached approximately 50 mm^3, these mice received a single intratumoral injection of 50 μL PBS, DOX (5 mg/kg), RD (containing 5 mg/kg DOX), MR, or MRD hydrogel (containing 5 mg/kg DOX). As shown in Figure 4C, the average tumor size in the PBS and MR groups increased rapidly and exceeded 1000 mm^3 at 16 days and 20 days, respectively. In contrast, all drug-treated groups exhibited obviously inhibited tumor growth levels. Treatment with the RD hydrogel suppressed tumor progression better than DOX up to 18 days after treatment, demonstrating that DOX released from the RD hydrogel displayed an enhanced antitumor effect *in vivo* due to the sustained release of DOX. More importantly, the MRD hydrogel showed significantly improved antitumor efficacy compared with the RD hydrogel, indicating the importance of backbone-loading with melittin for the anticancer effect of the MRD hydrogel. The MR hydrogel alone (without DOX loading) showed enhanced anticancer efficacy compared to PBS. At day 40, none of the tumored mice treated with PBS, DOX, RD, or MR survived, whereas 57% of MRD-treated mice remained tumor-free (Figure 4D). The administration of the MRD hydrogel significantly prolonged the survival of the mice (Figure 4E). These data suggest that the MRD hydrogel is a potent *in vivo* antitumor agent, which is attributed to backbone-loaded melittin and the sustained release of DOX.

***In Vivo* Peritumoral Administration of MRD Hydrogel.** Next, we treated subcutaneous B16-F10 tumor-bearing mice with different MRD hydrogel doses through peritumoral injection. When the tumor volume reached about 40 mm^3, the mice received a single peritumoral injection of 50 μL PBS, DOX, RD, or MRD hydrogel, with a DOX dose of 5 and 10 mg/kg. As depicted in Figure 5A, the PBS group showed a rapid tumor growth rate, and the tumor size exceeded 1000 mm^3 at 8 days post-treatment. As expected, all drug-treated groups showed obvious tumor growth inhibition. No dose effect was observed in the DOX-treated group, while the RD hydrogel-treated group displayed significant differences between the doses of 5 and 10 mg/kg, with tumor-inhibition rates of 70 and 95%, respectively. Administration of the MRD hydrogel exhibited the highest inhibitory efficacy against B16-F10 tumors. In regard to the dose effect, treatment with 10 mg/kg MRD hydrogel (98%) resulted in a slightly higher tumor-inhibition rate than treatment with 5 mg/kg MRD hydrogel (94%); however, this difference was not statistically significant. Thus, we chose a dose of 5 mg/kg MRD hydrogel for the

DOI: 10.1021/acsnano.7b08148
ACS Nano XXXX, XXX, XXX−XXX

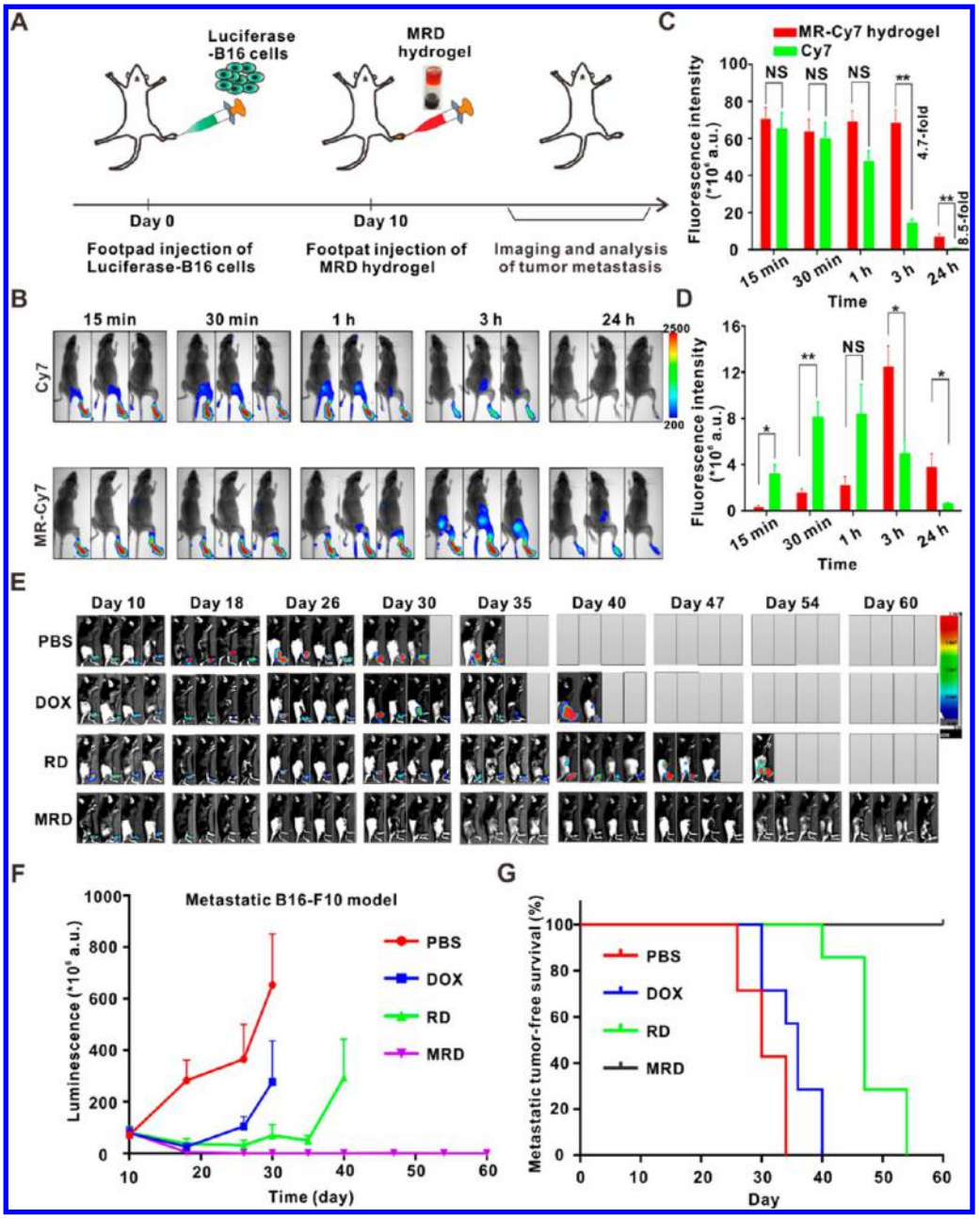

Figure 7. ***In vivo*** **metastasis inhibition effects of MRD hydrogel. (A) Schematic illustration of the MRD hydrogel treatment plan to inhibit tumor metastasis. (B)** ***In vivo*** **NIR fluorescence imaging of the distribution of MR-Cy7 hydrogel or Cy7 dye after footpad injection at various time points. (C,D) Quantification of the fluorescence signals of both footpads (C) and PLNs (D) in each group. (E)** ***In vivo*** **bioluminescence images to monitor the growth and spreading of footpad-injected B16-Luc cells in different groups of mice. (F) Averages of the quantified bioluminescence signals in each group. (G) Survival percentages in the corresponding treatment groups described in (E). Data are presented as the mean ± SEM (*n* = 6).**

following *in vivo* studies. The dissected tumors are shown in Figure 5B, and their weight was measured. We found that the MRD hydrogel had significantly higher anticancer activity than PBS, DOX, and RD hydrogel at both tested DOX concentrations (Figure 5C). These results were consistent with hematoxylin-eosin (HE) staining, TUNEL assay, and Ki67 staining, which showed that treatment with the MRD hydrogel resulted in the highest level of necrotic lesions, the highest apoptosis rate, and the lowest level of proliferative capacity, respectively (Figure 5D).

To evaluate the biocompatibility of the MRD hydrogel, we recorded the tumor weight changes; hemanalysis and biochemical analyses were performed on blood withdrawn from the mice on day 8 post drug treatment; and normal tissues, such as heart, liver, spleen, lung, and kidney, were dissected for histopathological analyses. During the study period of 8 days, mice treated with the MRD hydrogel (5 or 10 mg/kg) remained normal, as indicated by the absence of major behavioral changes or weight loss (Figure S8). At a DOX concentration of 5 mg/kg, all drug-treated groups and the PBS control showed similar levels of hemoglobin (HGB), platelet (PLT) number, red and white blood cell (WBC and RBC) number (Figure 6A), monocyte, lymphocyte, and neutrophil granulocyte number (Figure S9), and heart and renal function

DOI: 10.1021/acsnano.7b08148
ACS Nano XXXX, XXX, XXX−XXX

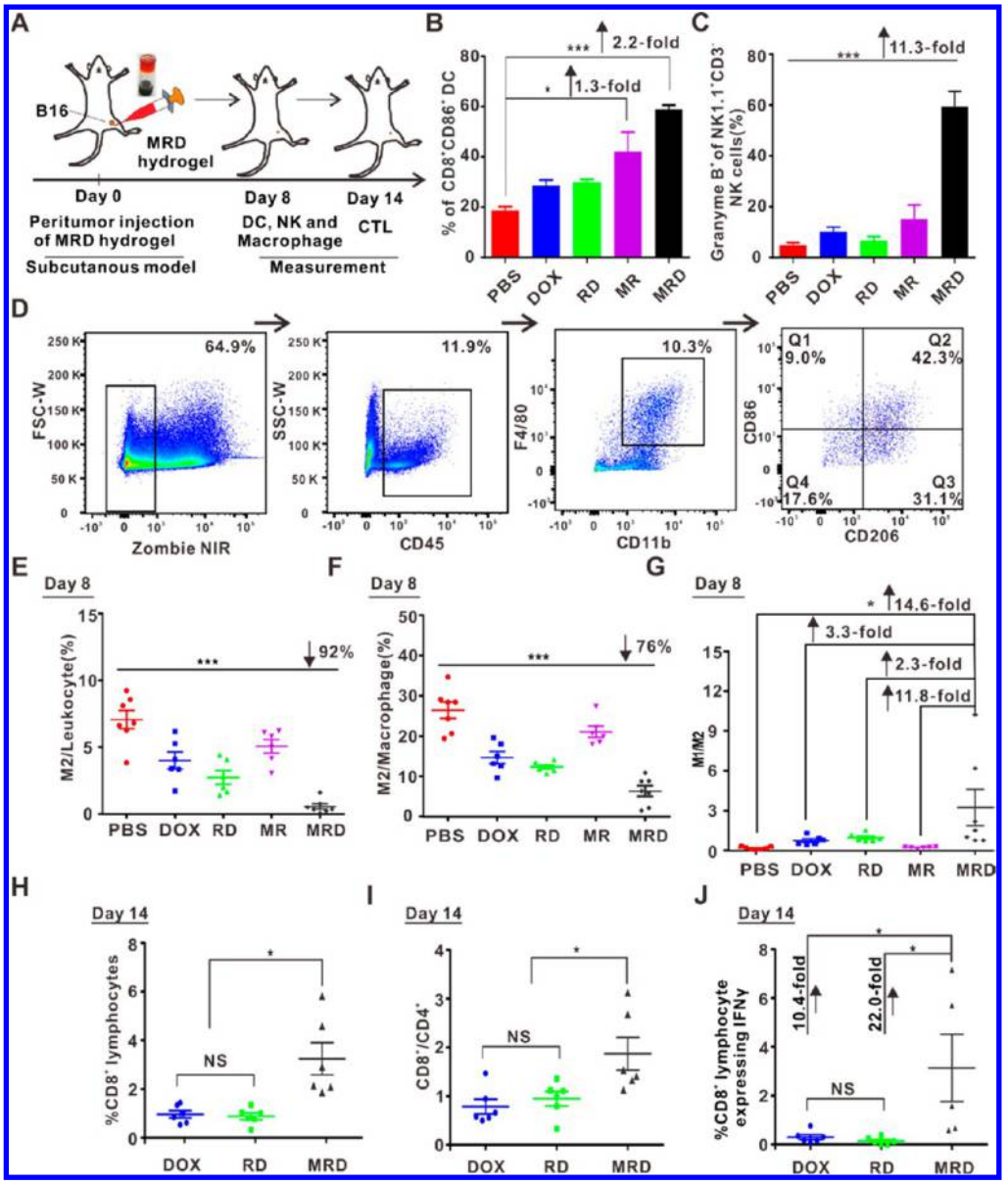

Figure 8. ***In vivo*** **immune activation effects of MRD hydrogel. (A) Schematic illustration of the MRD hydrogel treatment plan for immune analysis. (B) Percentages of activated DCs ($CD11c^+CD80^+CD86^+$) within PLNs. (C) Percentages of activated NKs (granzyme $B^+NK1.1^+CD3^-$) within tumors. (D) Flow cytometry gating strategy for measurement of M1-like ($CD45^+CD11b^+F4/80^+CD86^+CD206^-$) and M2-like TAMs ($CD45^+CD11b^+F4/80^+CD86^-CD206^+$). Data are presented as the mean ± SEM (n = 5 or 6) for (A–D). (E–G) Percentages of the M2/leukocyte (E), M2/total macrophages (F), and M1/M2 ratios (G) within tumors of the different treatment groups. (H) Percentages of $CD8^+$ T cells within tumors in each group. (I) Ratios of $CD8^+$ to $CD4^+$ T cells within tumors in each group. (J) Portions of cytotoxic $CD8^+$ IFNγ^+ T cells within tumors in each group. Data are presented as the mean ± SEM (n = 6) for (E–J).**

parameters (such as creatine kinase (CK) and total bilirubin (T-Bil)). We observed that the PBS group had abnormal levels of glutamic pyruvic transaminase (ALT), glutamic oxaloacetic transaminase (AST), and lactic dehydrogenase isoenzyme (LDH-1), while these parameters remained normal in DOX, RD hydrogel, and MRD hydrogel-treated mice, possibly due to the larger tumor burden in the PBS group. Post-mortem histopathological examination of heart, liver, spleen, lung, and kidney demonstrated that these organs remained in normal condition and were not affected by the MRD hydrogel in the dose used in this study (Figure 6B).

In Vivo **Metastasis Inhibition Effects of MRD Hydrogel.** Cancer metastases are extremely detrimental to cancer patients and often highly correlated with poor survival, as they can hardly be cured through conventional therapies. Therefore, we next investigated whether the MRD hydrogel is effective in the treatment of a more aggressive lymphatic metastasis tumor. In this model, B16-F10 cells stably expressing firefly luciferase (B16-Luc) were subcutaneously inoculated into the mouse footpad and allowed to grow for 10 days. These mice were then subjected to footpad injection of PBS, DOX, RD, or MRD hydrogel, and tumor growth and metastasis were monitored by whole-body fluorescence imaging (Figure 7A). Prior to this study, in order to assess the *in vivo* biodistribution of the drug after footpad-injection with MRD hydrogel, we used MR-Cy7 hydrogel to mimic the MRD hydrogel. When the free Cy7 dye was subcutaneously injected into the mouse footpad, it exhibited a strong fluorescence signal at 15 and 30 min. At 1

DOI: 10.1021/acsnano.7b08148
ACS Nano XXXX, XXX, XXX–XXX

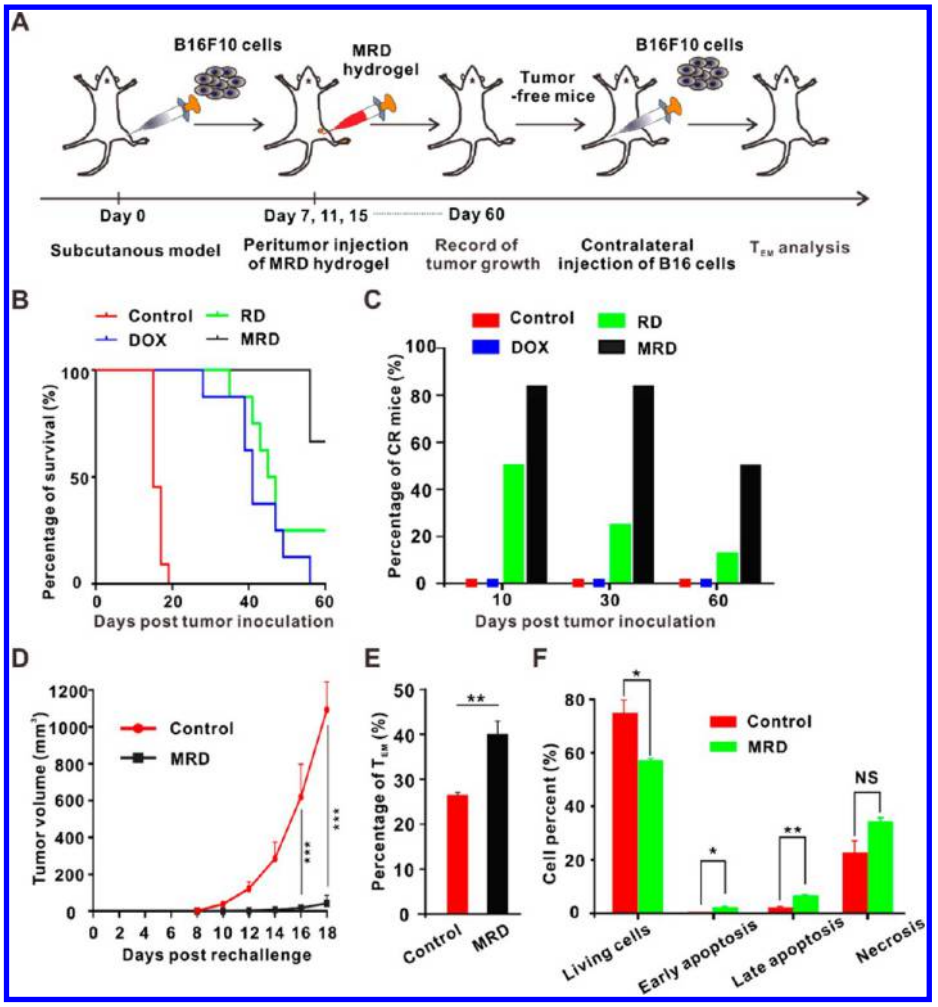

Figure 9. Long-term immune-memory effects of MRD hydrogel. (A) Schematic illustration of the MRD hydrogel treatment plan for the analysis of immune-memory effects. (B) Survival percentages in the corresponding treatment groups. Data are presented as the mean ± SEM (n = 6 to 11). (C) Percentages of CR mice in each group. (D) Quantification of the second tumor growth. (E) Proportions of splenic T_{EM} ($CD3^+CD8^+CD44^+$) cells. (F) Flow cytometry of B16-F10 cell apoptosis induced by splenic cells isolated from mice treated with MRD hydrogel or PBS. Data are presented as the mean ± SEM (n = 3 to 4).

and 3 h, this signal extensively dropped by 26.5% and 69.8%, respectively, and became almost undetectable at 24 h (Figure 7B,C). In contrast, MR-Cy7 hydrogel-treated footpads displayed an intensive fluorescence signal at 15 min, which remained for at least 3 h without any attenuation. Even at 24 h, the signal remained detectable. Statistical data showed that the signals of mouse footpads injected with MR-Cy7 hydrogel were 4.7- and 8.5-fold stronger than those of the Cy7 group at 3 and 24 h, respectively. Moreover, the fluorescence signals of the mouse popliteal lymph node (PLN) in each group showed a similar trend (Figure 7D). These data indicate that in the footpad model, the MRD hydrogel may provide an enhanced sustained release of DOX due to the similarity of MRD and MR-C7 hydrogels.

In the therapeutic footpad model, before PBS, DOX, RD, or MRD hydrogel had been administered, mice in these groups had very similar bioluminescence signal levels at the footpads 10 days post B16-Luc cell inoculation. A representative photograph of a mouse footpad at 18 days showed obvious tumor growth in the PBS and DOX groups (Figure S10). In the PBS control group, mice showed strong bioluminescence signals at the footpad and obvious cancer metastasis 26 days after tumor inoculation (Figure 7E). For the DOX and RD hydrogel groups, primary footpad tumors presented a relatively slower growth rate (Figure 7F); metastases also occurred, but at later stages. In contrast, the primary tumors of mice treated with the MRD hydrogel were eradicated, and no metastasis occurred even at 60 days post tumor inoculation (Figure 7E). The survival curve clearly shows that mice that received PBS and DOX all died within 25−40 days, and all RD hydrogel-treated mice developed metastases within a relatively longer time of 54 days (Figure 7G). However, mice injected with the MRD hydrogel displayed 100% survival, indicating that the MRD hydrogel could be a promising antimetastasis agent.

Immune Activation of MRD Hydrogel. After confirming the acceptable biocompatibility and strong antitumor activity of the MRD hydrogel, we next investigated whether the MRD hydrogel could trigger rapid innate and adaptive immune responses *in vivo*. In this experiment, the subcutaneous B16-F10 tumor-bearing mice were peritumorally treated with PBS, DOX, RD, MR, or MRD hydrogel. At 8 days post-treatment, lymph node (LN) DCs, NKs, and macrophages in the tumors were analyzed by flow cytometry, followed by cytotoxic T lymphocyte (CTL) analysis at day 14 post-treatment (Figure 8A). The antitumor effects of the MRD hydrogel are shown in Figure S11. At day 8, inguinal LNs (ILNs) of the treated mice

DOI: 10.1021/acsnano.7b08148
ACS Nano XXXX, XXX, XXX−XXX

were collected, and the expression levels of CD11c, CD80, and CD86 were analyzed. As shown in Figures S12A and 8B, cell expression of $CD11c^+CD80^+CD86^+$, which indicates mature DCs, was significantly elevated in the MR and MRD hydrogel-treated group as compared to other groups (Figure 8B). Moreover, this effect was not observed in DOX or RD hydrogel-treated groups, excluding the role of DOX or RD hydrogel backbone in mediating DC maturation. Combined with the *in vitro* stimulation effect of the MRD hydrogel on DCs (Figure 3E-G), these results together revealed the unique impact of the MRD hydrogel on stimulating the maturation of resident DCs within the LNs. Additionally, we observed that the administration of MRD hydrogel caused the greatest increase in the proportions of granzyme $B^+NK1.1^+CD3^-$ cells (Figure S12B), which indicates the presence of activated NKs within tumor tissues in contrast to other controls. When compared to the PBS group, the MRD hydrogel group exhibited an 11.3-fold increase of the proportion of local, activated NKs (Figure 8C), indicating that the MRD hydrogel triggered rapid innate immune responses *in vivo*.

As the MRD hydrogel effectively treats melanoma cells, we wondered if the MRD hydrogel could destroy M2-like TAMs, which play an important role in promoting tumor progression and metastasis within TMEs. The gating strategy for M1- and M2-like TAMs, indicated by $CD45^+CD11b^+F4/80^+CD86^+CD206^-$ and $CD45^+CD11b^+F4/80^+CD86^-CD206^+$ cells, respectively, is demonstrated in Figure 8D. At day 8, we observed a significant decline (92%) of the ratio of M2-like TAMs to total leukocytes (M2/Leukocyte) within tumors collected from MRD hydrogel-treated mice compared with PBS controls (Figure 8E). Furthermore, the MRD hydrogel group displayed a 76% decrease of the ratio of M2-like TAMs to total TAMs (M2/Macrophages) compared with the PBS control (Figure 8F). The MRD hydrogel group exhibited the highest ratio of M1-like to M2-like TAMs (M1/M2), which was 14.6-fold higher than that of the PBS group (Figure 8G). Additionally, we found that the population of leukocytes and M1-like TAMs was not affected by this depletion effect, while it showed a slight increase in the MRD hydrogel group compared with PBS control (Figure S13). Together, these results indicate that the MRD hydrogel has the potential to specifically deplete M2-like TAMs.

As the generation of a significant number of CTLs often required a relatively longer time, another batch of mice was evaluated at day 14 post drug administration. Since all mice in the PBS group died (average volume >1000 mm^3), we compared the levels of $CD8^+$ T cells within tumors among the DOX, RD hydrogel, and MRD hydrogel groups. We found that the portion of $CD8^+$ T cells and $CD4^+$ T cells in the MRD hydrogel group was significantly higher than those in the DOX and RD hydrogel groups (Figure 8H, Figure S14A,B), and the ratio of $CD8^+$ to $CD4^+$ T cells was consistent with this result (Figure 8I). More crucially, we observed that the portion of cytotoxic $CD8^+$ IFNγ^+ T cells in the MRD hydrogel group was 10.4- and 22.0-fold higher than that in the DOX and RD hydrogel groups, respectively (Figure 8J, Figure S15). Additionally, the cytokine production in peripheral blood was measured. This revealed that MRD hydrogel treatment augmented the serum levels of IFN-γ and IL-2, the major antitumor cytokines, in contrast to treatment with DOX or RD hydrogel (Figure S16), indicating that the MRD hydrogel mediated the production of IFN-γ and IL-2. Together, these results reveal that MRD hydrogel treatment induced the infiltration and accumulation of a large portion of CTLs in the tumors and contributed to the production of antitumor cytokines.

Long-Term Immune-Memory Effects of MRD Hydrogel. As the MRD hydrogel has potent antitumor activity and triggers rapid innate and adaptive immune responses, we hypothesized that the MRD hydrogel could generate an antitumor immune memory. To evaluate this, subcutaneous B16-F10 tumor-bearing mice were peritumorally injected with PBS, DOX, RD, RADA, MR, or MRD hydrogel every 4 days for three times in total, and the tumor growth was recorded for 60 days (Figure 9A). As shown in Figure 9B and Figure S17, all mice died in the PBS, RADA, and MR groups at day 24. At days 40 and 60, DOX, RD hydrogel, and MRD hydrogel-treated mice had a survival rate of 62.5% and 0%, 87.5% and 25%, 100% and 67%, respectively. Moreover, the percentage of mice exhibiting complete regression (CR) reached 50% at day 60 in the MRD hydrogel-treated group, but only 0 and 12.5% in the DOX and RD hydrogel-treated groups, respectively, suggesting that the MRD hydrogel has the capacity to eradicate existing tumors (Figure 9C).

Next, CR mice in the MRD hydrogel group and normal control healthy mice were subcutaneously injected with B16-F10 cells at their contralateral flanks, and their growth was monitored. Results showed that the contralateral tumors in the MRD hydrogel group had a delayed growth rate compared with that of PBS control mice. At day 18 post tumor inoculation, the tumor volume of the control mice exceeded 1000 mm^3, while the MRD hydrogel group had an average tumor volume of 30 mm^3 (Figure 9D), suggesting the presence of memory cells. To confirm this speculation, spleens harvested from MRD hydrogel-treated mice or the control group were analyzed. Flow cytometry analysis showed that the percentage of splenic $CD3^+CD8^+CD44^+$ cells (Figure S18), which stain for effector memory T cells (T_{EM}), was significantly elevated in the MRD hydrogel group compared with the PBS group (Figure 9E), confirming the importance of the MRD hydrogel in the production of a large portion of T_{EM} cells. When the splenic cells collected from these two groups were separately incubated with B16-F10 cells, the MRD hydrogel group displayed a significantly enhanced cell-killing effect toward B16-F10 cells compared with the PBS group (Figure 9F). Collectively, these results demonstrate that the MRD hydrogel is favorable for the generation of memory immune responses after eradication of primary melanoma tumors.

DISCUSSION

Immunosuppressive TMEs constructed mainly by lymphatic vessels, tumor cells, fibroblasts, and a variety of immune cells often bring tremendous obstacles for effective cancer therapy, and established TMEs can hardly be reversed through conventional therapies. Due to the TMEs' heterogeneous properties and complicated cell−cell communication networks, it is often difficult to reshape the immune profile of the TMEs to improve the anticancer efficacy by using single treatment modalities;[7,33] thus, multidimensional treatment planning is often required. Here, we developed a simple melittin/DOX-containing hybrid peptide hydrogel (MRD hydrogel) system for potent chemoimmunotherapy against melanoma with both subcutaneous and metastasis tumors through TME modulation. MRD hydrogel offers a melittin and DOX-based direct cell-killing effect, depletion of M2-like macrophages, generation of

DOI: 10.1021/acsnano.7b08148
ACS Nano XXXX, XXX, XXX−XXX

rapid innate and adaptive immune responses, as well as long-term immune-memory effects.

The central component of the MRD hydrogel is melittin, a bee venom-derived cationic polypeptide with 26 amino acids. In order to make melittin applicable for *in vivo* anticancer purposes, several studies have recently attempted to integrate melittin into biomaterials to reduce its hemolysis effect.[40−43] In this study, the hemolysis effect of melittin could be reduced by constructing a $RADA_{32}$-melittin fusion peptide and, more significantly, by the formation of cross-linked nanofibers. In this context, we introduced an alternative approach for the application of melittin. The unique role of melittin in the potent *in vivo* tumor inhibition mediated by the MRD hydrogel was demonstrated at least by the following aspects: (1) direct killing effect to tumor cells. We observed that the MRD hydrogel, in combination with melittin and DOX, induced cell necrosis *in vitro* (Figure 2E), mainly through rapid membrane disruption and inhibition of cell cycle progression (Figure 3A,D); (2) activation of DCs and initiation of adaptive immune responses. DC maturation is an essential process for antigen presentation and subsequent T cell activation. We reported that MR hydrogel promotes DC maturation *in vitro*, which indeed depends on melittin, because the $RADA_{16}$ hydrogel did not show this effect (Figure S19). Moreover, the MRD hydrogel effectively stimulated the DCs in the draining LNs (DLNs) (Figure 8B). In contrast to other DC-targeting nanovaccines that require the addition of immune-stimulating agents (*e.g.*, CpG oligonucleotides and monophosphoryl lipid A), the MRD hydrogel itself could potentially act as an effective immune-stimulating adjuvant, which in turn contributes to T cell activation; (3) depletion of M2-like TAMs. It is now well recognized that M2-like TAMs are appealing therapeutic target because they often promote key events in tumor progression, such as angiogenesis, immunosuppression, invasion, and metastasis.[44] However, specific depletion of M2-like TAMs remains challenging, and to date only a mere handful of approaches (*e.g.*, peptide-functionalized lipid nanoparticles and antibodies against CSF-1R) have been shown successful.[45,46] In this study, we provided an effective approach for the depletion of M2-like TAMs: on the one hand, neither free DOX nor RD hydrogel showed such a potent effect; on the other hand, we found that the MRD hydrogel-induced depletion of M2-like TAMs occurred without concomitant reduction of the population of M1-like TAMs within the tumors (Figure S13).

Peptide hydrogels, formed by designer amphiphilic self-assembling peptides or hydrogelators, have been widely used in biomedical applications, such as 3D tissue cell culture, tissue engineering, regenerative medicine, and cancer treatment.[35,47−49] Using the MRD hydrogel for *in vivo* tumor inhibition or ablation may provide the following advantages: (1) controlled drug release. We clearly observed by fluorescence imaging that the release rate of Cy7 dye loaded onto the MR-Cy7 hydrogel was decreased in both subcutaneous and footpad models (Figures 4A and 7B). The controlled drug release could be indeed translated into enhanced therapeutic efficacy, as revealed by the significantly enhanced tumor inhibition rate of the MRD and RD hydrogels compared with that of free DOX. Additionally, the drug release rate of the MRD hydrogel can potentially be further tailored to adapt to different therapeutic demands by altering the salt or peptide concentration; (2) synergistic inhibition effect. The development of drug resistance, which is regulated by multidrug resistance-associated proteins in the tumor membrane, is a major roadblock to successful cancer treatment. However, this barrier may be potentially circumvented by using MR hydrogel platforms, because the MR hydrogel could disrupt cell membrane functions and may increase the accessibility of loaded drugs to tumor cells. Likewise, MR hydrogel platforms may be well-suited for the treatment of cancer stem cells; (3) immune-stimulating ability. Compared with other hydrogel systems, such as alginate and polypeptide hydrogels, the MRD hydrogel scaffold possesses strong immune-stimulating ability without the need of cytokines, immune checkpoint inhibitors, and immune-stimulating adjuvants; (4) ease of synthesis. The MRD hydrogel could be simply described as a complexes of one peptide and DOX, both of which can be easily produced in a large scale; (5) excellent stability, biocompatibility, and biodegradability. The MR hydrogel is composed of saline and peptides, which have been proven to be biodegradable in response to proteinase K treatment, and it is stable for at least 3 months at 4 °C (data not shown); (6) versatile drug-loading capacity. We have proven that the MR hydrogel could be loaded with various types of drugs or fluorescent dyes, which can be either hydrophilic or hydrophobic agents (Figure 1B). Moreover, drug-loading efficiency of nearly 100% could be achieved with these agents, ensuring a broad range of biomedical applications.

The MRD hydrogel represents a powerful localized treatment platform for tumors through multiple therapeutic mechanisms, such as direct cell killing, regulation of macrophage differentiation, and generation of adaptive immune responses. For clinical cancer treatment, the MRD hydrogel can also be combined with systemic immunotherapy (*e.g.*, CAR-T and checkpoint-blockade therapy) or radiotherapy to further improve the therapeutic index. Another potential application may be the prevention of local tumor recurrence after surgical resection in patients with different cancer types, including glioblastoma, breast cancer, and osteogenic sarcoma. For this application, the MRD hydrogel can be directly injected into the residual cavity to treat invisible residual lesions by exerting sustained drug release and immune stimulation. Thus, our future work will focus on seeking after broader application of our MRD hydrogel system.

CONCLUSION

Immune repressive TMEs represent a tremendous barrier for effective cancer treatment. In this study, we developed a powerful peptide hydrogel, MRD hydrogel, which encapsulates melittin in the hydrogel backbone and DOX in the hydrogel matrix. This peptide hydrogel was designed for potent combination therapy against melanoma through remodeling immune repressive TMEs. Due to its controlled drug release property and its abilities to regulate innate immune cells, deplete M2-like TAMs, and direct anticancer and immune stimulation, the MRD hydrogel exhibits potent anticancer efficacy for subcutaneous and metastasis tumors. The MRD hydrogel could be further used to eradicate melanoma *in vivo* and induce strong immunological memory effects to serve as a powerful tool for anticancer applications.

EXPERIMENTAL SECTION

Materials. $RADA_{16}$ peptide (Ac-RADARADARADARADA-NH_2) and $RADA_{32}$-melittin fusion peptide (Ac-RADARADARADARADAR-ADARADARADARADA-GG-GIGAVLKVLTTGLPALIS-WIKRKRQQ-NH_2) were synthesized by Bankpeptide Ltd. (Hefei,

DOI: 10.1021/acsnano.7b08148
ACS Nano XXXX, XXX, XXX−XXX

China). Doxorubicin (Catalog: 25316-40-9) was purchased from Aladdin (Shanghai, China).

Hydrogel Synthesis. DOX solution (2 mg/mL) was obtained by dissolving DOX powder in 0.9% NaCl solution at room temperature. To prepare DOX-loaded MR or MRD hydrogel, 10 mg MR peptide was dissolved in 1 mL DOX solution (2 mg/mL) and subjected to repeated pipetting for complete dissolution. This mixture was kept at 4 °C for overnight, resulting in the formation of the MRD hydrogel. DOX-loaded $RADA_{16}$ or RD hydrogel was prepared in the same manner by replacing the MR peptide by the equal amount of $RADA_{16}$ peptide. All steps were performed under sterile conditions.

Mice and Cells. Female C57BL/6 mice (6−8 weeks old) were purchased from HBCDC (Wuhan, China). All animals were raised in a specific pathogen-free barrier facility. All animal studies were performed in compliance with protocols that had been approved by the Hubei Provincial Animal Care and Use Committee, following the experimental guidelines of the Animal Experimentation Ethics Committee of the Huazhong University of Science and Technology (HUST, Wuhan, China). B16-F10 cells were kindly provided by Professor Zhihong Zhang (HUST, Wuhan, China). All cells were maintained in RPMI 1640 medium (Gibico) with 10% fetal bovine serum (FBS; Gibico) and 1% antibiotics (penicillin and streptomycin) in an atmosphere of 5% CO_2 at 37 °C.

Therapeutic Setting. To establish the B16-F10 tumor model, 5×10^5 B16-F10 cells in 100 μL 0.9% NaCl were injected subcutaneously into the right flank of each mouse. Seven days after inoculation, mice were divided into four groups (5−8 mice in each group): (a) 0.9% NaCl alone (50 μL), (b) DOX alone (50 μL), (c) RD (50 μL, 2 mg/mL DOX, 1.6 mM $RADR_{16}$ peptide), and (d) MRD (50 μL, 2 mg/mL DOX, 1.6 mM MR peptide). The mice were treated by intratumoral, peritumoral, or footpad injection. The tumor size was measured every 2 days using a caliper, and the tumor volume was calculated according to the following formula: volume = $\text{width}^2 \times \text{length}/2$. The mice were sacrificed at 8 or 14 days post-injection. To evaluate the therapeutic efficacy of the treatments, tumors and major tissues, including liver, heart, lung, spleen, and kidney, were harvested for HE analysis.

TEM Imaging of the Hydrogel. TEM was used to detect the morphology and structure of the MR and MRD hydrogels. Both hydrogels were diluted with ultrapure water at the ratio of 1:20. A hydrogel sample volume of 5 μL was dropcasted onto the clean surface of a copper grid, which was incubated for 2 min. Then, the liquid was dried by a bibulous paper. Subsequently, the sample was stained with 5 μL of phosphotungstic acid (5%) for 30 s, followed by drying with a bibulous paper. Then, the grids were imaged by TEM (Titan G2 60-300; FEI Company, OR).

***In Vitro* Gel Degradation and Drug Release.** *In vitro* gel degradation and drug release were performed by adding 0.5 mL MR or MRD hydrogel to the bottom of a 1.5 mL Eppendorf tube, and 1 mL 0.9% NaCl with or without 5 unit/mL proteinase K was added on top of the hydrogel layer at 37 °C. The top buffer was replaced by fresh buffer at the indicated time points and collected to detect the concentration of DOX. The remaining mass was accurately weighed every day. The collected buffer samples were analyzed using a fluorospectrophotometer (F97XP15007; Shanghai Lengguang Technology Co., Ltd., China) at an excitation wavelength of 500 nm and an emission wavelength of 550 nm.

Cell Viability Study. B16-F10 cells (5000 cells/well) were seeded in a 96-well plate with 100 μL culture medium and allowed to grow for 24 h before treatment. Then, the medium was replaced by 90 μL fresh culture medium and 10 μL of 0.9% NaCl. Into each plate, DOX (containing 10 μg/mL DOX), RD (containing 10 μg/mL DOX and 80 μM $RADA_{16}$), or MRD (containing 10 μg/mL DOX and 80 μM MR) hydrogel were added. The culture medium of these groups was changed daily. After incubation for 1, 3, 5, and 7 days at 37 °C, the cell viability was evaluated by the CCK8 assay.

Flow Cytometry Analysis of Apoptosis. B16-F10 cells (3×10^5 cells/well) were seeded in 6-well plates with 2 mL culture medium and incubated for 24 h before treatment. Then, 40 μL 0.9% NaCl, DOX (containing 50 μg/mL DOX), RD (containing 50 μg/mL DOX and 1.6 mM $RADA_{16}$), and MRD (containing 50 μg/mL DOX and 1.6 mM MR) were added. After incubation for 24 h, a cell suspension with a cell density of 1×10^6/mL was made by digestion with 0.25% trypsin without EDTA, followed by PBS washing and resuspension in 200 μL binding buffer. Subsequently, 5 μL annexin V-FITC and 5 mL PI solution (Beyotime Biotechnology) were added and incubated for 10 min before flow cytometry.

Bioluminescence. *In vivo* bioluminescence was detected by intraperitoneal injection of 150 mg/kg firefly luciferin (Thermo Life, CAS: 103404-75-7). After 15 min, the mice were anesthetized with 200 μL 1% pentobarbital sodium solution. Bioluminescence was measured with a Spectral Instruments Imaging Optical Imaging Platform (Lago X, Cold Spring Biotech Corp.; 20 s exposure). The average signal intensities within a circular region of interest (ROI) were quantified.

Confocal Imaging. To directly visualize MR hydrogel-medicated cell-killing, B16-GFP cells were seeded in a glass-bottom cell culture dish (NEST, Catalog: 801001; 1×10^5/well) and incubated for 24 h. Subsequently, these cells were incubated with Hoechst 33342 nuclear staining dye (0.5 μg/mL) for 10 min, followed by three times washing with PBS. Then, 1 mL culture medium containing 20 μL MR hydrogel and 2 μL PI were added to the dish. Fluorescent images were acquired using a fluorescence confocal microscope (Nikon A1R/A1) with an excitation wavelength of 405 nm for Hoechst 33342, 480 nm for GFP, and 535 nm for PI at each time point.

Hemolysis Assay. RBCs isolated from fresh mouse blood were collected and diluted to a cell density of 5×10^7/mL, and 100 μL of these RBCs was incubated with various concentrations of MR peptide or MR hydrogel at 37 °C for 4 h. Untreated RBCs suspended in PBS buffer were set as negative control for hemolysis; for the positive hemolysis control, RBCs were suspended in 1% Triton X-100. After centrifugation for 10 min, the supernatants from each group were measured by a microplate reader (Tecan Group Ltd., Mannedorf, Switzerland) at 540 nm.

Flow Cytometry Analysis of Cell Cycle. B16-F10 cells were seeded into 6-well plates (2×10^5/well) in triplicate with 2 mL culture medium (2×10^5/well). After 24 h, 40 μL of 0.9% NaCl, DOX (containing 50 μg/mL DOX), RD (containing 50 μg/mL DOX), or MRD hydrogel (containing 50 μg/mL DOX) was added into the plates for each group and allowed for treatment for 24 h. Cells were collected and fixed with 1 mL precooled 70% alcohol for 12 h. Subsequently, cells were washed with PBS and digested using RNA enzyme for 30 min at 37 °C. At last, 2 μL PI solution (initial concentration: 5 mg/mL) was added. After 10 min, cell cycle analysis was performed by flow cytometry.

Generation of BMDCs. Bone marrow-derived dendritic cells (BMDCs) were harvested from femurs and tibiae of 8−10 weeks old C57BL/6 male mice. After depleting RBCs by RBC lysis buffer, the cells were cultured in RPMI 1640 medium supplemented with 10% FBS and 20 ng/mL GM-CSF (PeproTech). Cytokines were replenished on days 3 and 5, and the resulting nonadherent cells were harvested for experiments.

Rheological Analysis. The rheological properties of MRD hydrogel were measured on a rheometer (DHR-2, TA, Instruments, New Castle, DE). The frequency sweep experiment was performed using a 1% (w/w) hydrogel. The storage modulus (G') and loss modulus (G'') were detected keeping strain at 0.1% with a continuous frequency (0.1−100 rad/s). To examine the thixotropic property of MRD hydrogel, 1% (w/w) hydrogel was used at a constant frequency of 1 rad/s. The MRD hydrogel was first measured under low constant strain of 0.1% for the initial 200 s, followed with a higher strain of 40% to destroy the gel matrix. Subsequently, the strain was adjusted to a constant low level of 0.1%, and the restoration process was recorded.

DC Maturation Analysis. To detect the effects of MR hydrogel on the maturation of DCs, imDCs were seeded into 24-well plates (1.5×10^5/well) with 1 mL culture medium. Then various concentration of solid MR hydrogel was added. After 24 h of incubation, the phenotype of DCs was detected. To detect the effects of MR hydrogel-induced tumor cell death on the maturation of DCs, B16 cells were treated with solid MR hydrogel for various time (0−48 h), and cell

DOI: 10.1021/acsnano.7b08148
ACS Nano XXXX, XXX, XXX−XXX

supernatants were collected, followed with 24 h incubation with imDCs. After that the phenotype of DCs was detected.

Immunohistochemistry. Melanoma biopsies in different groups were immunostained with mouse antibody for Ki67 (CST). After three times washing, secondary rabbit antimouse immunoglobulin G (IgG) conjugated to a horseradish peroxidase (CST) was added to the biopsies. After PBS washing, the biopsies were stained with 100 μL 3,3′-diaminobenzidine and counterstained with hematoxylin.

Flow Cytometry Analysis. For phenotypic analysis of DCs, BDMCs or cells prepared form draining LNs were stained with surface antibodies: anti-CD11c (clone N418), anti-CD80 (clone 16-10A1), and anti-CD86 (clone GL-1). To detect tumor-infiltrating T cells (TILs), tumor tissues were digested to prepare single cell suspensions and stained with antibodies against antimouse anti-CD3ε (clone 145-2C11), anti-CD4 (clone GK1.5), and anti-CD8a (clone 53-6.7). For intracellular cytokine staining, cell suspensions prepared from tumors were stimulated with ionomycin (1 mg/mL; Abcam) and phorbol 12-myristate 13-acetate (PMA; 50 ng/mL, Abcam) in the presence of bleomycin (1 mg/mL; Abcam) for 4 h. Subsequently, cells were stained with antibodies for surface staining. Next, cells were fixed and stained with anti-IFN-γ (clone XMG1.2). NK cells were detected using anti-CD3ε (clone 145−2C11), anti-NK1.1 (PK136), and antigranzyme B (GB11). For the phenotypic analysis of TAMs, cell suspensions made from tumor tissues were stained with the following surface antibodies: anti-CD45 (clone 30-F11), anti-CD11b (clone M1/70), anti-F4/80 (clone BM8), anti-CD80 (clone 16−10A1), and anti-CD86 (clone GL-1). Then, the cells were stained with anti-CD206 (c068C2) after fixation and permeabilization. For analysis of the memory cells, spleens harvested form mice were stained with anti-CD3ε (clone 145-2C11), anti-CD8a (clone 53-6.7), and anti-CD44 (clone IM7). All antibodies were purchased from Biolegend.

Cytokine Detection. Serum samples were isolated from each group and analyzed using a LEGENDplex Mouse Th1 Panel (5-plex; Catalog: 740025) according to the vendor's protocols.

Statistical Analysis. Student's *t*-test (two tailed) was used for statistical analysis of the *in vitro* studies. Tumor growth was analyzed applying the Kaplan−Meier method. Significant differences between the groups are indicated by * for $p < 0.05$, ** for $p < 0.01$, and *** for $p < 0.001$, respectively.

ASSOCIATED CONTENT

Supporting Information

The Supporting Information is available free of charge on the ACS Publications website at DOI: 10.1021/acsnano.7b08148.

The effects of the salt, peptide concentration, and pH on gel formation, comparison of the *in vitro* antitumor effects, quantitative data of the average number of living cells, evaluation of the *in vivo* mice weight changes, hemanalysis analyses, representative photograph of the mice footpad, measurement of *in vivo* immune activation effects, flow cytometry measurement of the M1-like TAMs, *in vivo* analysis of generation of adaptive immunity, *in vivo* analysis of the generation of $CD8^+$ IFN-γ^+ T cells, measurement of the serum cytokine levels in mice, flow cytometry gating strategy for the measurement of T_{EM} cells, and effects of the RADA hydrogel on DC maturation (PDF)

AUTHOR INFORMATION

Corresponding Authors

*E-mail: yangkunyu@medmail.com.cn.
*E-mail: xhzlwg@163.com.
*E-mail: chenjingunion@163.com.

ORCID

Zhenwei Zou: 0000-0002-3103-5519
Jonathan F. Lovell: 0000-0002-9052-884X
Kunyu Yang: 0000-0001-8570-6552

Author Contributions

⊥These authors contributed equally to this work.

Notes

The authors declare no competing financial interest.

ACKNOWLEDGMENTS

This study was conducted with the support by National Natural Science Foundation of China (grant no. 81503026 to J.H.; grant no. 81372435 to Y.K.; grant no. 8177111430 to C.J.), the Fundamental Research Funds for the Central Universities (HUST: 2015QN1), the Huazhong University of Science and Technology "Double Top" Construction Project of International Cooperation (grant 540-5001540013), and the National Key Research and Development Program of China (project no. 2016YFC0105300). We thank Dr. Guanxin Shen (HUST) for paper discussion. We thank the Center for Nanoscale Characterization & Devices (CNCD, Tecnai G20 U-Twin) of WNLO-HUST for the support in data acquisition.

REFERENCES

(1) Chen, D. S.; Mellman, I. Oncology Meets Immunology: the Cancer-Immunity Cycle. *Immunity* **2013**, *39*, 1−10.
(2) Danhier, F.; Feron, O.; Preat, V. To Exploit the Tumor Microenvironment: Passive and Active Tumor Targeting of Nanocarriers for Anti-cancer Drug Delivery. *J. Controlled Release* **2010**, *148*, 135−146.
(3) Taube, J. M.; Klein, A.; Brahmer, J. R.; Xu, H.; Pan, X.; Kim, J. H.; Chen, L.; Pardoll, D. M.; Topalian, S. L.; Anders, R. A. Association of PD-1, PD-1 Ligands, and Other Features of the Tumor Immune Microenvironment with Response to Anti-PD-1 Therapy. *Clin. Cancer Res.* **2014**, *20*, 5064−5074.
(4) Jain, R. K. Normalizing Tumor Microenvironment to Treat Cancer: Bench to Bedside to Biomarkers. *J. Clin. Oncol.* **2013**, *31*, 2205−2218.
(5) Swartz, M. A.; Iida, N.; Roberts, E. W.; Sangaletti, S.; Wong, M. H.; Yull, F. E.; Coussens, L. M.; DeClerck, Y. A. Tumor Microenvironment Complexity: Emerging Roles in Cancer Therapy. *Cancer Res.* **2012**, *72*, 2473−2480.
(6) Tredan, O.; Galmarini, C. M.; Patel, K.; Tannock, I. F. Drug Resistance and the Solid Tumor Microenvironment. *J. Natl. Cancer Inst.* **2007**, *99*, 1441−1454.
(7) Guo, S.; Lin, C. M.; Xu, Z.; Miao, L.; Wang, Y.; Huang, L. Co-delivery of Cisplatin and Rapamycin for Enhanced Anticancer Therapy through Synergistic Effects and Microenvironment Modulation. *ACS Nano* **2014**, *8*, 4996−5009.
(8) Hu, K.; Miao, L.; Goodwin, T. J.; Li, J.; Liu, Q.; Huang, L. Quercetin Remodels the Tumor Microenvironment to Improve the Permeation, Retention, and Antitumor Effects of Nanoparticles. *ACS Nano* **2017**, *11*, 4916−4925.
(9) Atkins, M. B. Cytokine-Based Therapy and Biochemotherapy for Advanced Melanoma. *Clin. Cancer Res.* **2006**, *12*, 2353s−2358s.
(10) Lin, W. W.; Karin, M. A Cytokine-Mediated Link between Innate Immunity, Inflammation, and Cancer. *J. Clin. Invest.* **2007**, *117*, 1175−1183.
(11) Hahn, A. W.; Gill, D. M.; Pal, S. K.; Agarwal, N. The Future of Immune Checkpoint Cancer Therapy after PD-1 and CTLA-4. *Immunotherapy* **2017**, *9*, 681−692.
(12) Sharma, P.; Allison, J. P. The Future of Immune Checkpoint Therapy. *Science* **2015**, *348*, 56−61.
(13) Qian, Y.; Jin, H.; Qiao, S.; Dai, Y.; Huang, C.; Lu, L.; Luo, Q.; Zhang, Z. Targeting Dendritic Cells in Lymph Node with An Antigen Peptide-Based Nanovaccine for Cancer Immunotherapy. *Biomaterials* **2016**, *98*, 171−83.
(14) Shi, G. N.; Zhang, C. N.; Xu, R.; Niu, J. F.; Song, H. J.; Zhang, X. Y.; Wang, W. W.; Wang, Y. M.; Li, C.; Wei, X. Q.; Kong, D. L.

DOI: 10.1021/acsnano.7b08148
ACS Nano XXXX, XXX, XXX−XXX

Enhanced Antitumor Immunity by Targeting Dendritic Cells with Tumor Cell Lysate-Loaded Chitosan Nanoparticles Vaccine. *Biomaterials* **2017**, *113*, 191−202.
(15) Zhu, G.; Zhang, F.; Ni, Q.; Niu, G.; Chen, X. Efficient Nanovaccine Delivery in Cancer Immunotherapy. *ACS Nano* **2017**, *11*, 2387−2392.
(16) Han, E. Q.; Li, X. L.; Wang, C. R.; Li, T. F.; Han, S. Y. Chimeric Antigen Receptor-engineered T Cells for Cancer Immunotherapy: Progress and Challenges. *J. Hematol. Oncol.* **2013**, *6*, 47.
(17) Jin, H.; Qian, Y.; Dai, Y.; Qiao, S.; Huang, C.; Lu, L.; Luo, Q.; Chen, J.; Zhang, Z. Magnetic Enrichment of Dendritic Cell Vaccine in Lymph Node with Fluorescent-Magnetic Nanoparticles Enhanced Cancer Immunotherapy. *Theranostics* **2016**, *6*, 2000−2014.
(18) Chen, Q.; Xu, L.; Liang, C.; Wang, C.; Peng, R.; Liu, Z. Photothermal Therapy with Immune-adjuvant Nanoparticles Together with Checkpoint Blockade for Effective Cancer Immunotherapy. *Nat. Commun.* **2016**, *7*, 13193.
(19) Hanahan, D.; Coussens, L. M. Accessories to the Crime: Functions of Cells Recruited to the Tumor Microenvironment. *Cancer Cell* **2012**, *21*, 309−322.
(20) Whiteside, T. L. The Tumor Microenvironment and Its Role in Promoting Tumor Growth. *Oncogene* **2008**, *27*, 5904−5912.
(21) Li, X.; Naylor, M. F.; Le, H.; Nordquist, R. E.; Teague, T. K.; Howard, C. A.; Murray, C.; Chen, W. R. Clinical Effects of *in Situ* Photoimmunotherapy on Late-stage Melanoma Patients: a Preliminary Study. *Cancer Biol. Ther.* **2010**, *10*, 1081−1087.
(22) Gajewski, T. F.; Schreiber, H.; Fu, Y. X. Innate and Adaptive Immune Cells in the Tumor Microenvironment. *Nat. Immunol.* **2013**, *14*, 1014−1022.
(23) Liu, E.; Tong, Y.; Dotti, G.; Shaim, H.; Savoldo, B.; Mukherjee, M.; Orange, J.; Wan, X.; Lu, X.; Reynolds, A.; Gagea, M.; Banerjee, P.; Cai, R.; Bdaiwi, M. H.; Basar, R.; Muftuoglu, M.; Li, L.; Marin, D.; Wierda, W.; Keating, M.; Champlin, R.; Shpall, E.; Rezvani, K. Cord Blood NK Cells Engineered to Express IL-15 and A CD19-targeted CAR Show Long-term Persistence and Potent Antitumor Activity. *Leukemia* **2018**, *32*, 520−531.
(24) Morvan, M. G.; Lanier, L. L. NK Cells and Cancer: You Can Teach Innate Cells New Tricks. *Nat. Rev. Cancer* **2016**, *16*, 7−19.
(25) Jiang, H.; Wang, Q.; Sun, X. Lymph Node Targeting Strategies to Improve Vaccination Efficacy. *J. Controlled Release* **2017**, *267*, 47−56.
(26) Mathios, D.; Kim, J. E.; Mangraviti, A.; Phallen, J.; Park, C. K.; Jackson, C. M.; Garzon-Muvdi, T.; Kim, E.; Theodros, D.; Polanczyk, M.; Martin, A. M.; Suk, I.; Ye, X.; Tyler, B.; Bettegowda, C.; Brem, H.; Pardoll, D. M.; Lim, M. Anti-PD-1 Antitumor Immunity Is Enhanced by Local and Abrogated by Systemic Chemotherapy in GBM. *Sci. Transl. Med.* **2016**, *8*, 370ra180.
(27) Whiteside, T. L. Immune Suppression in Cancer: Effects on Immune Cells, Mechanisms and Future Therapeutic Intervention. *Semin. Cancer Biol.* **2006**, *16*, 3−15.
(28) Zamarron, B. F.; Chen, W. Dual Roles of Immune Cells and Their Factors in Cancer Development and Progression. *Int. J. Biol. Sci.* **2011**, *7*, 651−658.
(29) Galon, J.; Costes, A.; Sanchez-Cabo, F.; Kirilovsky, A.; Mlecnik, B.; Lagorce-Pages, C.; Tosolini, M.; Camus, M.; Berger, A.; Wind, P.; Zinzindohoue, F.; Bruneval, P.; Cugnenc, P. H.; Trajanoski, Z.; Fridman, W. H.; Pages, F. Type, Density, and Location of Immune Cells within Human Colorectal Tumors Predict Clinical Outcome. *Science* **2006**, *313*, 1960−1964.
(30) Tosolini, M.; Kirilovsky, A.; Mlecnik, B.; Fredriksen, T.; Mauger, S.; Bindea, G.; Berger, A.; Bruneval, P.; Fridman, W. H.; Pages, F.; Galon, J. Clinical Impact of Different Classes of Infiltrating T Cytotoxic and Helper Cells (Th1, Th2, Treg, Th17) in Patients with Colorectal Cancer. *Cancer Res.* **2011**, *71*, 1263−1271.
(31) Li, Y.; Fang, M.; Zhang, J.; Wang, J.; Song, Y.; Shi, J.; Li, W.; Wu, G.; Ren, J.; Wang, Z.; Zou, W.; Wang, L. Hydrogel Dual Delivered Celecoxib and Anti-PD-1 Synergistically Improve Antitumor Immunity. *Oncoimmunology* **2016**, *5*, e1074374.
(32) Nishikawa, M.; Mizuno, Y.; Mohri, K.; Matsuoka, N.; Rattanakiat, S.; Takahashi, Y.; Funabashi, H.; Luo, D.; Takakura, Y. Biodegradable CpG DNA Hydrogels for Sustained Delivery of Doxorubicin and Immunostimulatory Signals in Tumor-Bearing Mice. *Biomaterials* **2011**, *32*, 488−494.
(33) Wu, X.; Wu, Y.; Ye, H.; Yu, S.; He, C.; Chen, X. Interleukin-15 and Cisplatin Co-Encapsulated Thermosensitive Polypeptide Hydrogels for Combined Immuno-Chemotherapy. *J. Controlled Release* **2017**, *255*, 81−93.
(34) Gelain, F.; Unsworth, L. D.; Zhang, S. Slow and Sustained Release of Active Cytokines from Self-Assembling Peptide Scaffolds. *J. Controlled Release* **2010**, *145*, 231−239.
(35) Luo, Z.; Zhang, S. Designer Nanomaterials Using Chiral Self-Assembling Peptide Systems and Their Emerging Benefit for Society. *Chem. Soc. Rev.* **2012**, *41*, 4736−4754.
(36) Bechinger, B. Structure and Functions of Channel-Forming Peptides: Magainins, Cecropins, Melittin and Alamethicin. *J. Membr. Biol.* **1997**, *156*, 197−211.
(37) Dempsey, C. E. The Actions of Melittin on Membranes. *Biochim. Biophys. Acta, Rev. Biomembr.* **1990**, *1031*, 143−161.
(38) Gao, W.; Zhang, Y.; Zhang, Q.; Zhang, L. Nanoparticle-Hydrogel: A Hybrid Biomaterial System for Localized Drug Delivery. *Ann. Biomed. Eng.* **2016**, *44*, 2049−2061.
(39) Baral, A.; Roy, S.; Dehsorkhi, A.; Hamley, I. W.; Mohapatra, S.; Ghosh, S.; Banerjee, A. Assembly of An Injectable Noncytotoxic Peptide-Based Hydrogelator for Sustained Release of Drugs. *Langmuir* **2014**, *30*, 929−936.
(40) Huang, C.; Jin, H.; Qian, Y.; Qi, S.; Luo, H.; Luo, Q.; Zhang, Z. Hybrid Melittin Cytolytic Peptide-Driven Ultrasmall Lipid Nanoparticles Block Melanoma Growth *in Vivo*. *ACS Nano* **2013**, *7*, 5791−5800.
(41) Jin, H.; Zhao, G.; Hu, J.; Ren, Q.; Yang, K.; Wan, C.; Huang, A.; Li, P.; Feng, J. P.; Chen, J.; Zou, Z. Melittin-Containing Hybrid Peptide Hydrogels for Enhanced Photothermal Therapy of Glioblastoma. *ACS Appl. Mater. Interfaces* **2017**, *9*, 25755−25766.
(42) Kim, M. G.; Shon, Y.; Kim, J.; Oh, Y. K. Selective Activation of Anticancer Chemotherapy by Cancer-Associated Fibroblasts in the Tumor Microenvironment. *J. Natl. Cancer Inst.* **2017**, *109*, djw186.
(43) Soman, N. R.; Lanza, G. M.; Heuser, J. M.; Schlesinger, P. H.; Wickline, S. A. Synthesis and Characterization of Stable Fluorocarbon Nanostructures as Drug Delivery Vehicles for Cytolytic Peptides. *Nano Lett.* **2008**, *8*, 1131−1136.
(44) De Palma, M.; Lewis, C. E. Macrophage Regulation of Tumor Responses to Anticancer Therapies. *Cancer Cell* **2013**, *23*, 277−286.
(45) Ngambenjawong, C.; Gustafson, H. H.; Pun, S. H. Progress in Tumor-Associated Macrophage (TAM)-Targeted Therapeutics. *Adv. Drug Delivery Rev.* **2017**, *114*, 206−221.
(46) Qian, Y.; Qiao, S.; Dai, Y.; Xu, G.; Dai, B.; Lu, L.; Yu, X.; Luo, Q.; Zhang, Z. Molecular-Targeted Immunotherapeutic Strategy for Melanoma *via* Dual-Targeting Nanoparticles Delivering Small Interfering RNA to Tumor-Associated Macrophages. *ACS Nano* **2017**, *11*, 9536−9549.
(47) Yu, C. Y.; Huang, W.; Li, Z. P.; Lei, X. Y.; He, D. X.; Sun, L. Progress in Self-Assembling Peptide-Based Nanomaterials for Biomedical Applications. *Curr. Top. Med. Chem.* **2016**, *16*, 281−290.
(48) Basu, K.; Baral, A.; Basak, S.; Dehsorkhi, A.; Nanda, J.; Bhunia, D.; Ghosh, S.; Castelletto, V.; Hamley, I. W.; Banerjee, A. Peptide Based Hydrogels for Cancer Drug Release: Modulation of Stiffness, Drug Release and Proteolytic Stability of Hydrogels by Incorporating D-Amino Acid Residue(s). *Chem. Commun.* **2016**, *52*, 5045−5048.
(49) Naskar, J.; Palui, G.; Banerjee, A. Tetrapeptide-Based Hydrogels: for Encapsulation and Slow Release of an Anticancer Drug at Physiological pH. *J. Phys. Chem. B* **2009**, *113*, 11787−11792.

DOI: 10.1021/acsnano.7b08148
ACS Nano XXXX, XXX, XXX−XXX